8-2015

ANALYSIS AND AN APPLICATION OF RF INTERFEROMETER

Yongzhi Shao
Clemson University, yongzhs@clemson.edu

ANALYSIS AND AN APPLICATION OF RF INTERFEROMETER

A Thesis
Presented to
the Graduate School of
Clemson University

In Partial Fulfillment
of the Requirements for the Degree
Master of Science
Electrical Engineering

---

by
Yongzhi Shao
August 2015

Accepted by:
Pingshan Wang, Committee Chair
Anthony Martin
Rod Harrell

ABSTRACT

The thesis investigates additive RF interferometer sensing technique, which is highly sensitive compared to other RF sensing methods. First, mathematical descriptions are given to illustrate how the RF interferometer works. Then an analysis of single particle passing over a coplanar waveguide in carrier liquid is presented, which poses as a difficulty to simulation software. The analysis is combined with interferometer mathematical equations and validated by a particle measurement in an interferometer. The interferometer sensitivity is enhanced by incorporating filters as sensing devices and functionally expanded by using the reflection coefficients. In the end, an application of gas measurement with the RF interferometer is presented. The test system is built and preliminary results are obtained, which provides guidance for future work.

ACKNOWLEDGMENTS

The work in the thesis would not be possible without the help of many people. First of all, I would especially like to thank my advisor Dr. Pingshan Wang for all the time and efforts he spent on helping me during my two years of study in Clemson University. His knowledge, ideas and thinking on applied electromagnetics, along with the advice, guidance and encouragement, are very helpful for the accomplishment of my research projects and personal growth as well.

I would like to express my gratitude to my committee members, Dr. Anthony Martin and Dr. Rod Harrell for being my committees. Their comments on my dissertation are very valuable. The lectures given by them gave me knowledge of fundamentals in electromagnetics and semiconductor devices and they are pleasant memories of Clemson University.

I would also like to thank my group members and many friends for their kind help. Special thanks to Dr. Jiwei Sun for being such a nice person and all the help on every aspect since the very beginning at Clemson. The inspiring discussions and selfless help I had from all group members are greatly appreciated. It is an honor to be part of the group and work with you guys.

Lastly, I would like to thank my parents for the support of my life choice, tolerance of the burden I have brought to the family, and their love which carried me through all the happy and hard days.

TABLE OF CONTENTS

Page

Table of Contents (Continued)

Page

LIST OF TABLES

Table

Page

LIST OF FIGURES

Figure

Page

List of Figures (Continued)

Page

CHAPTER ONE

INTRODUCTION

RF sensors have been widely investigated for all kinds of applications such as process control [1.1], automobile speed and collision avoidance [1.2], biological and chemical sensing [1.3], etc. RF method has many merits other methods cannot achieve. For instance, in the biological and medical fields, it is possible to achieve non-invasive and real time measurement *in vivo* [1.4]. In indoor ranging, RF identification is low-cost for mass production and effectively reduces the required computational resources compared to image or video monitoring methods [1.5]. With the development of high speed solid state electronics, RF sensors have been developed and commercialized in a compact and cost effective way. However, the low resolution remains a problem and challenge for the RF sensors using direct measurements.

The RF interferometer is a unique RF sensor that provides unprecedented high resolution and sensitivity. As it literally implies, it interferes two signals to form a more sensitive signal when material under test (MUT) is introduced compared to direct measuring. The interferometry technique starts from the optical Michaelson interferometer and most interferometer achievements reside in the optical area. Due to the high resolution of the interferometry method, RF interferometer has been intensively applied in astronomy and radar applications. For ease of integration with circuit technology, RF interferometer mainly uses a mixer to multiply two signals, which bring noise from active devices.

In our system, the interferometer contains only passive devices and removes possible sources of active noise. Destructive interference based on additive signals, which has a very small magnitude and sensitive to changes, is used. The system has been applied to dielectric and cell measurements and demonstrates very high sensitivity. It is capable of obtaining MUT properties measurement results. Our efforts on the additive RF interferometer applications are discussed with more details in chapter II.

The thesis is organized as following:

Chapter II introduces the development of RF interferometry technique and our efforts on it. A detailed analysis is given for the operations of RF interferometer. The analysis could model the frequencies at which the lowest minima would happen. It predicts the frequency and magnitude shifts when MUT is introduced as well. The interferometer operation is expanded to include the reflection operation. More general cases that happen in experiments are discussed. Equations that calculate the quasi-quality factor of the minima are presented as well.

Chapter III proposes a method that is capable of analyzing a particle or cell passing in a microfluidic channel over a coplanar waveguide (CPW), which is difficult to analyze with simulation software. The electrical and magnetic field patterns are plotted analytically with conformal mapping method. The analysis based on the field patterns is given then with details. Measurement results with the RF interferometer agree to the results from analysis.

In chapter IV, two CPW based filters are designed to enhance the local electrical field and interaction time, thus to improve the interferometer sensitivity. Interferometer

measurement results, including transmission and reflection operations, are presented to validate the model given in chapter II. Measurement results are compared to the modeled results by plugging the broadband data into the system model. We also retrieve MUT permittivity from measurement results. The results show some agreements and deviations as well. Further work is needed to improve the accuracy of the proposed method.

Chapter V presents an application of the RF interferometer: volatile organic components measurement.

REFERENCES

[1.1] Sohraby, Kazem, Daniel Minoli, and Taieb Znati. *Wireless sensor networks: technology, protocols, and applications*. John Wiley & Sons, 2007.

[1.2] Hulderman, Garry N. "RF sensor and radar for automotive speed and collision avoidance applications." *U.S. Patent* No. 5,486,832. 23 Jan. 1996.

[1.3] Taylor, Richard F., and Jerome S. Schultz, eds. *Handbook of chemical and biological sensors*. CRC Press, 1996.

[1.4] Jean, B. Randall, Eric C. Green, and Melanie J. McClung. "A microwave frequency sensor for non-invasive blood-glucose measurement." *Sensors Applications Symposium, IEEE*, 2008.

[1.5] Ma, Yunfei, and Edwin C. Kan. "Accurate Indoor Ranging by Broadband Harmonic Generation in Passive NLTL Backscatter Tags." *Microwave Theory and Techniques, IEEE Transactions on* 62.5 (2014): 1249-1261.

CHAPTER TWO

RF INTERFEROMETER ANALYSIS

In this chapter, we start from the origin of interferometry technique and introduce the applications and development of RF interferometer. Then the development and applications of the RF interferometer we use is briefly introduced. In section 2.2 how the RF interferometer works is discussed in detail and the general mathematical equations describing the RF interferometer are given.

2.1 Introduction to RF Interferometer

Interferometry is an extensively used technique based on the superimposition of two waves to extract useful information with high sensitivity. It is more sensitive compared with direct measuring. The ripple pattern from the interference of two stones falling into water is a natural example of interferometry. The first engineering application of the interferometer can be traced to the Michaelson interferometer in the 19th century, which gave birth to the later optical interferometers [2.1]. With the advent of electronics, interferometry served as the fundamental of some radar [2.2] and radio astronomy technologies [2.3], which use mixers to multiply two signals, and provides superior sensitivity that direct measuring cannot achieve. In astronomy, a resolution of an arc second (1/3600 degree) has been achieved by a radio interferometer which could work in a broader RF bandwidth than optical method which is limited only to the visible light

bandwidth [2.4]. The interferometer using a mixer in the system architecture is also used to measure phase and amplitude noise [2.5] and spatial displacement [2.6].

Our RF interferometer uses all passive components, such as power divider and quadratic hybrid instead of mixer, as shown in Fig. 2.1 (a), to superimpose the two split signals for high sensitivity measurement, which eliminates the noise of active components. The sensor could be a uniform transmission line, a filter or a resonator in different situations. The power divider could be replaced by quadrature hybrid. R_1 and R_2 are attenuators and Φ_1 and Φ_2 are phase shifters. The components are connected by coaxial cables and stabilized on a table. We can have one sensor in one branch or have two sensors in both branches. Fig. 2.1 (b) shows a typical built interferometer.

The basic idea of our interferometer is to make the signals, either transmission or reflection, of the two branches cancel each other at certain frequencies, thus forming a minimum level of -80 or -100 dB to amplify the changes caused by the material under test (MUT). In this way, magnitude change of 0.0001 or even 0.00001 could be reflected from the measurement results if we could make sure the measured changes are indeed caused by the MUT. The small magnitude change is difficult to measure directly since it is smaller than the uncertainty level of network analyzer. Our interferometer started as an on-chip device, however not tunable [2.7]. The device has been applied to distinguish live and dead yeast cells passing through a microfluidic channel [2.8]. Later, the interferometer is developed as an off-chip system containing multiple components as in Fig. 2.1 [2.9]. A major application is to measure dielectric liquids. 0.05 mg/mL glucose solution could be distinguished from water [2.10].

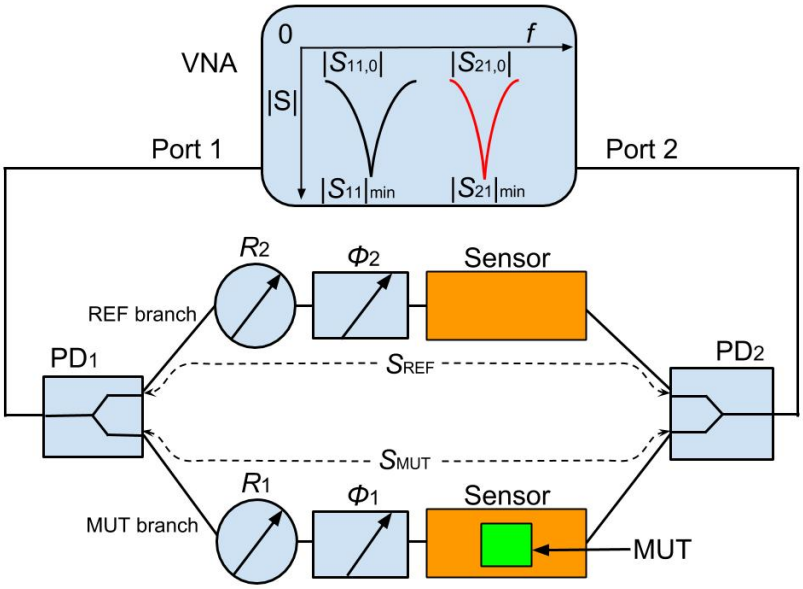

(a)

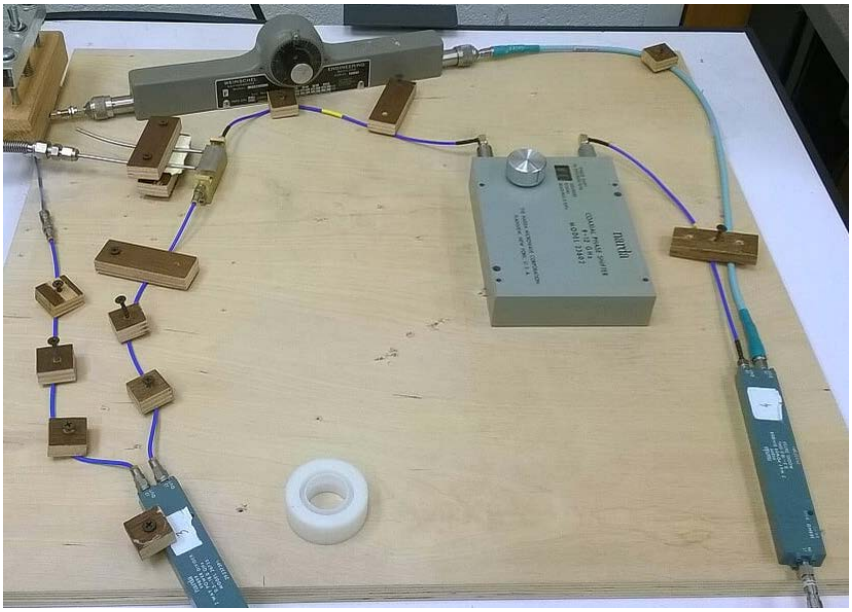

(b)

Fig. 2.1 (a) A Schematic and (b) photo of the RF interferometer.

The same architecture as what we use is adapted by some other groups. For example, the interferometer is applied to keep track of yeast cell viability [2.11]. The RF interferometer with only one hybrid quadrature measuring reflection has been applied to measure extremely large impedance [2.12] and sub-femto Farad capacitance [2.13].

2.2 Analysis of RF Interferometer

In this section, equations describing how the interferometer works are given. We start from the transmission operation and analyze the more general cases. The quasi-quality factor is calculated and a data fitting process is given.

2.2.1 Transmission Operation of Interferometer

Consider the transmission RF signal in Fig. 2.1, which originates from power divider 1 and observed at power divider 2. Then the transmitted signals of the MUT and REF branches can be written as

$$\boldsymbol{S}_{MUT} = A_1 e^{-\mathrm{j}\beta_1 l_1 - j\Phi_0}; \boldsymbol{S}_{REF} = A_2 e^{-\mathrm{j}\beta_2 l_2 - j\Phi_0} \tag{2.1}$$

where A_1 and A_2 are the magnitude of transmission coefficients and they could be frequency dependent since the system components and the connections are not ideal. The equivalent transmission lines of length $l_{1,\ 2}$ and phase propagation constants $\beta_{1,\ 2}$ are assumed for the branches. There will be reflections in the connecting junctions and they have been incorporated in A_1 and A_2 in (2.1). Φ_0 is the non-zero initial phase at DC frequency for some filters and resonators and it could be factored out if the sensors in the two branches are symmetrical, which is recommended for simple analysis.

When the first minimum happens at hundreds MHz or even lower, A_1 and A_2 can be assumed frequency independent in an operation band where the one measurement is conducted. The operation band is usually on the order of several MHz or smaller. Fig. 2.2 is an example of the magnitude and phase slope with frequency in an operation frequency bandwidth and it shows that such assumptions are reasonable since phase slope with frequency of two branches in an operation bandwidth is much larger than magnitude change as shown. Then we can write the interferometer output $|\boldsymbol{S}_{21}|$ as

$$|\boldsymbol{S}_{21}(f)| = \frac{1}{2}\left|A_1 + A_2 e^{-\mathrm{j}\Phi(f)}\right| \tag{2.2}$$

where Φ is the electrical length difference between the two branches; the factor 1/2 is due to power dividers or quadrature hybrids. For example, the *S* matrix of power divider is

$$\boldsymbol{S} = -\frac{\mathrm{j}}{\sqrt{2}}\begin{bmatrix} 0 & 1 & 1 \\ 1 & 0 & 0 \\ 1 & 0 & 0 \end{bmatrix} \tag{2.3}$$

Assuming the input is V^+, the input is split into two equal parts of -0.707jV^+. Then the output is

$$-\frac{v^+}{2}\left(A_1 e^{-\mathrm{j}\Phi_1} + A_2 e^{-\mathrm{j}\Phi_2}\right) \tag{2.4}$$

which justifies the half factor in the (2.2). Amplitude change in one branch will be halved in the final output. One potential way to make amplitude changes more obvious is to use imbalanced power divider. The Wilkinson power divider at the output end lets even mode signal pass and dissipates odd mode signal. We can write the two branch signals as a sum of even and odd signal, with the even part going through lossless and odd part dissipated by the 100 Ohm resistor in the power divider. Therefore, when A_1 is around -A_2 (the destructive interference), the majority of power is absorbed by the resistor with minimal

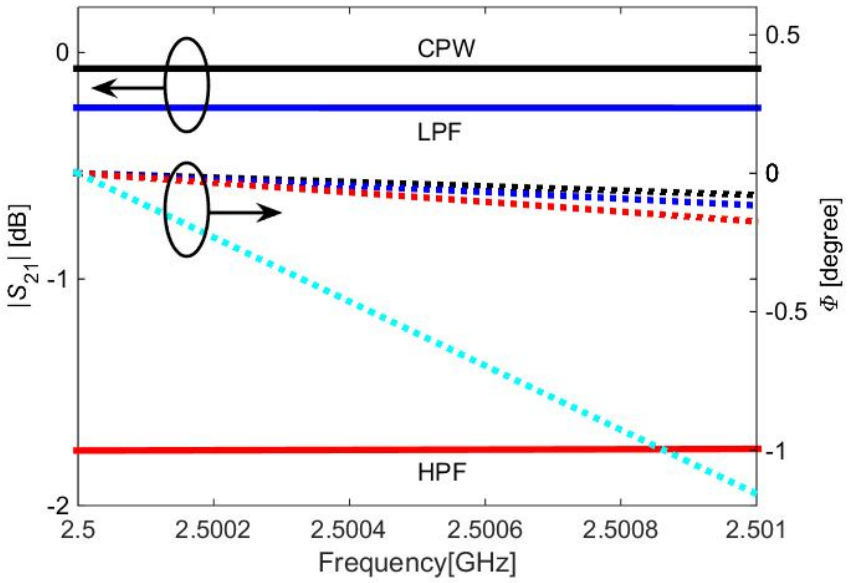

Fig. 2.2 Magnitude (solid lines) and phase (dashed lines) of the sensors in an operation frequency band. The phase of the two branch length difference is shown as the cyan dashed line.

output. When A_1 is around A_2 (the constructive interference), the power suffers no loss due to the power divider thus can achieve almost 0 dB in the output. For the case of hybrid quadrature, most energy is dissipated in the terminated resistor.

For Φ we have

$$\Phi = \beta_1 l_1 - \beta_2 l_2 = \left(\frac{2\pi l_1}{v_{p1}} - \frac{2\pi l_2}{v_{p2}}\right) f = Cf \tag{2.5}$$

where $v_{p1,2}$ are the equivalent phase velocities. The coefficient C in (2.5) can be considered as a constant in an operation frequency band.

If A_1 and A_2 are not strongly frequency dependent as in Fig. 2.2, $|\boldsymbol{S}_{21}|_{\min}$ occurs at frequencies where the two branches have a phase difference of

$$\Phi = (2n-1)\pi \tag{2.6}$$

Equating (2.5) and (2.6), we can predict the frequencies where $|\boldsymbol{S}_{21}|_{\min}$ happen or calculate C from measured $|\boldsymbol{S}_{21}|_{\min}$ frequencies. n =1 in (2.6) is considered as the fundamental operating frequency f_1 of the interferometer. The rest frequencies are marked as f_n in the thesis. When MUT is introduced on the sensing area, the sensor induces phase and magnitude changes, i.e. $\Delta\Phi$ and ΔA. $\Delta\Phi$ will lead to a frequency shift Δf to compensate the phase change and satisfy the relation of (2.6). Then we have

$$C(f+\Delta f) - \Delta\Phi = (2n-1)\pi;\ C\Delta f = \Delta\Phi \tag{2.7}$$

If $\Delta\Phi$ is known, such as from direct broadband measurements, then the interferometer frequency shift Δf can be predicted with (2.7). On the other hand, the measured Δf can be used to obtain $\Delta\Phi$, further to obtain MUT properties.

Equation (2.7) shows that the interferometer in Fig. 2.1 has higher frequency sensitivity, i.e. larger Δf for a given MUT $\Delta\Phi$, when operating at its fundamental frequency f_1. If a second interferometer also operates at f_1, but with $n\neq1$, then the coefficient C will be ($2n$-1) times larger. Correspondingly, the electrical length difference of the two branches in the second interferometer is ($2n$-1) times that of the first interferometer. Therefore, its Δf will be ($2n$-1) times smaller, as reported in [2.14]. More measurement results are reported in chapter IV.

One may wonder the minimum phase shift the interferometer could detect. If the 1st minimum happens at 1 GHz and we detect a trustworthy frequency shift of 10 kHz, then 0.0018° change happens on the sensor. It means that the interferometer could detect phase change to the order of 0.001. Another program is written to find the corresponding

permittivity change. A 50 Ohm CPW with 10 μm gap is assumed for the program. We also assume that MUT has a height of 412 μm and length of 472 μm from the example paper [2.15]. Then it is found that the 0.001° phase change corresponds to a permittivity change from 1 to 1.01.

The magnitude of $|\boldsymbol{S}_{21}|_{\min}$ is half of the difference between A_1 and A_2

$$|\boldsymbol{S}_{21}(f_0)|_{min} = \frac{1}{2}|A_1(f_0) - A_2(f_0)| \tag{2.8a}$$

Assume the MUT induced loss that modifies A_1 to A_1 (1+α), then (2.6a) becomes

$$|\boldsymbol{S}_{21}(f)|_{min,MUT} = \frac{1}{2}|A_1(f_0) - A_2(f_0) + \alpha A_1(f_0)| \tag{2.8b}$$

Equation (2.8) shows that larger A_1 and better balance between A_1 and A_2 yield higher magnitude sensitivity. In measurements the magnitude changes are usually accompanied by frequency shift. For example, for a system with a starting level of -60 dB, when MUT is introduced the MUT branch magnitude is A_1' from A_1 with f_n shifting to f_n', then the output could be written as

$$|\boldsymbol{S}_{21}(f_n')|_{min} = \frac{1}{2}|A_1(f_n') - A_1(f_n) + A_1(f_n) - A_2(f_n')| \approx \left|\frac{1}{2}|\Delta A_1| \pm 0.001\right| \tag{2.9}$$

There is an ambiguity to the sign of (A_1 - A_2). For example both ±0.001 contribute to a $|\boldsymbol{S}_{21}|_{\min}$ of -60 dB. Thus, precautions should be taken in measurements to make sure that such ambiguity is avoided and $\Delta|\boldsymbol{S}_{21}|_{\min}$ can be used to obtain MUT information. In measurements, efforts are made to make all minimum go up. If $\Delta|\boldsymbol{S}_{21}| > 0$, i.e. MUT makes $|\boldsymbol{S}_{21}|$ better; the attenuation of attenuator should be larger than the ideal point so that the minimum can always go up. Thus +0.001 is used in the analysis. If $\Delta|\boldsymbol{S}_{21}|$

< 0, i.e. MUT makes $|\boldsymbol{S}_{21}|$ worse; the attenuation of attenuator should be smaller than the ideal point so that the minimum can always go up. Thus -0.001 is used in the analysis.

We mainly focus on the magnitude from the *S* parameter measurement. The phase characteristic sees a sudden change of π at $|\boldsymbol{S}_{21}|_{\min}$. They have the same resolution in terms of reading the corresponding frequency.

2.2.2 Reflection Operation of Interferometer

The arrangement of the components in Fig. 2.1 allows the tuning of $\boldsymbol{S}_{21}$ and $\boldsymbol{S}_{11}$ separately. $\boldsymbol{S}_{11}$ becomes tunable compared to the system reported in [2.16]. $\boldsymbol{S}_{21}$ and $\boldsymbol{S}_{11}$ can be tuned simultaneously to a desired level and to a desired frequency. In stop-band, filter or resonator has large insertion loss and large reflection, i.e. $|\boldsymbol{S}_{21}| \approx 0$ and $|\boldsymbol{S}_{11}| \approx 1$. Destructive interference between the strong reflected waves from the two filters or resonators in each branch can be achieved at port 1 at a desired operating frequency in stop-band by tuning the phase shifters along the reflected RF wave paths. Actually, the reflection from dielectric liquid measurement as in [2.10] and [2.16] with uniform transmission lines is large enough to be used in reflection operation. The attenuators can tune $|\boldsymbol{S}_{11}|_{min}$ to a desired level. However, the arrangement in Fig. 2.1 makes it difficult to use S_{22} since no tuning mechanisms are available for $\boldsymbol{S}_{22}$.

For $\boldsymbol{S}_{11}$ measurement, the analysis of transmission operation in 2.2.1 is also valid except the electrical length doubles for a certain cable length since the reflected wave propagates forward and bounces backward from the unmatched position. Therefore, the Φ in (2.2) has different physical meaning. Reflections between the power divider and

vector network analyzer (VNA) port 1 also need to be incorporated in the equation and it required that the power divider has decent match. Power dividers could be replaced by quadrature hybrids and they function similarly.

2.2.3 General Analysis of Interferometer Transmission Operation

However, the analysis of section 2.2.1 fails when A_1 and A_2 are strongly frequency dependent. A_1 and A_2 in (2.1) should be written as A_1 (f) and A_2 (f) in reality. A possible source of strong frequency dependence is the sharp skirts of filters or resonators. All possible situations to (2.2) are categorized according to the number of frequency dependent variables in Table 2.1.

Case 1 is exactly the case we analyzed in 2.2.1. Case 2 is the situation where, one of the magnitudes, e.g., A_1 and the phase different Φ are frequency independent. Then we can write the output as

$$\boldsymbol{S}_{21}(f) = \frac{1}{2}\left|A_1 + A_2(f)e^{-\mathrm{j}\Phi}\right| \tag{2.10a}$$

For ease of analysis, we find the square of (2.9a) as below when Φ is around -π

$$|\boldsymbol{S}_{21}(f)|^2 = \frac{1}{4}[A_1 - A_2(f)]^2 + \frac{1}{4}A_1A_2(f)\Phi^2 \tag{2.10b}$$

According to law of cosine, when A_2 (f) = $A_1\cos\Phi$ the output is minimum

$$|\boldsymbol{S}_{21}(f)|^2_{min} = \frac{1}{4}A_1^2 sin^2\Phi \tag{2.11}$$

Fig. 2.3 is an example of this situation. It happens when the first $|\boldsymbol{S}_{21}|_{min}$ corresponding frequency is large, for example around 3 GHz as in the Fig. 2.3 and a magnitude frequency dependent filter is used in MUT branch. The minimum shifts up

TABLE 2.1

All cases of interferometer in terms of frequency dependent variables (marked by tick).

Case	A_1	A_2	Φ
1			✓
2		✓	
2	✓		
	✓	✓	
3		✓	✓
3	✓		✓
4	✓	✓	✓

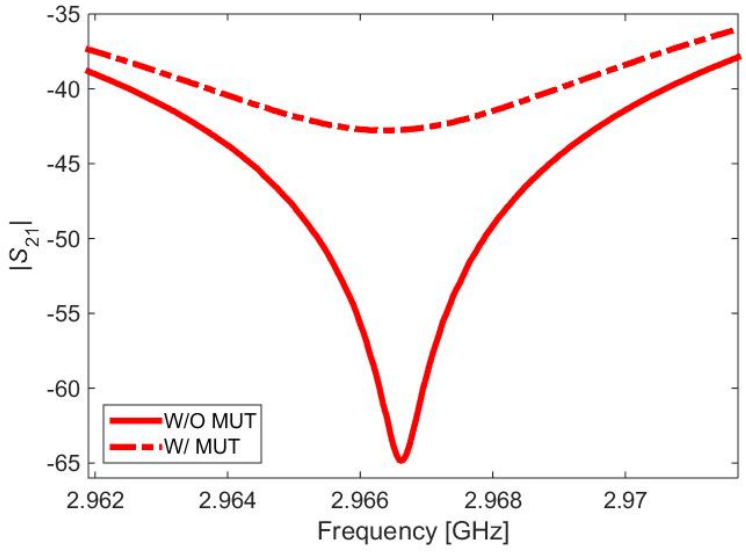

Fig. 2.3 Measurement results of $|S_{21}|_{min}$ when f_0 is ~ 2.95 GHz.

and down instead of left and right when phase change happens on the sensor as shown. This is verified by the equations above. The analysis also explains why two adjacent minima close to each other are observed in measurement since it is possible that multiple frequency points are satisfactory of the condition of (2.11).

Case 3 is the situation in which one of the magnitudes, e.g., A_1 is constant and the rest are frequency dependent. Case 4 is the situation that all variables are frequency dependent. Case 3 and 4 are combinations of case 1 and 2. In reality, the system will be case 3 or 4, which can dissembled to the sum of case 1 and 2 and it is very complex to analyze. However, we could approximate the practical system to case 1 or 2 for analysis in measurement: when 2 branch electrical length different is large and dominant, the constant magnitude assumption, i.e. case 1, is valid; when 2 branch electrical length come closer and the magnitude frequency dependence is dominant, case 2 has to be considered. Fig. 2.2 is an example of approximation to case 1 and it is reasonable since the magnitude variations are much smaller than the phase variation.

2.2.4 Quasi-Quality Factor of Interferometer

For the interferometer in section 2.2.1, the $|\boldsymbol{S}_{21}|_{min}$ we use has a nominal quality factor, i.e. the ratio of the center frequency f_n to the 3-dB bandwidth. However, the quality factor here is different from the physical definition of quality factor defined by stored and dissipated energy since there is no energy storing mechanism in the interferometer. The quasi-Q of the interferometer can be extremely high even to the order of 10^6, as reported in [2.17], which is higher than that of most traditional resonators.

The $|\boldsymbol{S}_{21}|_{min}$ magnitude is half the difference of A_1 and A_2. Then the 3 dB frequency will be as follows from (2.10)

$$cos[\Phi(f_{3dB})] = \frac{A_1^2+A_2^2-4A_1A_2}{2A_1A_2} = \frac{|A_1-A_2|^2}{2A_1A_2} - 1 = B \tag{2.12}$$

Then with the f_n from (2.5), (2.6), and (2.11), we can find Q as

$$Q = \frac{f_n}{\Delta f_{3dB}} = \frac{f_n}{2[f_n - f(cos^{-1}B)]} = \frac{(2n-1)\pi}{2\left[(2n-1)\pi - \frac{2\pi\Delta l}{v_p} f(cos^{-1}B)\right]} \tag{2.13}$$

The coefficient in (2.5) is simplified by assuming the two branches have the same phase velocity. B gets closer to -1 as $|A_1\text{-}A_2|$ gets smaller. Then the 3 dB frequency gets closer to f_n which leads to larger Q. From (2.13) we can also see that Q is large when n is large for a certain frequency when the magnitude level is the same. These support the conclusions that lower magnitude and larger n lead to a higher quasi-quality factor.

2.2.5 Data Fitting of Measured Interferometer Results

The measured S parameter from VNA of the interferometer is in the form of logarithm and Fig. 2.4 (a) presents a typical measurement curve at -90 dB. The curve is similar to the lower half of a logarithm curve, mirrored at the operation frequency. Fig. 2.4 (b) is the same curve, but with absolute data value. We can see that after returning the logarithm values to absolute values, the curve has linear trends on both sides.

An interferometer is usually operated at a very low level, such as -90 dB in Fig. 2.4(a). This level is easily affected by the ambient environment, such as mechanical vibrations and electromagnetic radiations from wireless communications. Therefore, fluctuations might appear around the operation frequency point as in Fig. 2.4(a) and

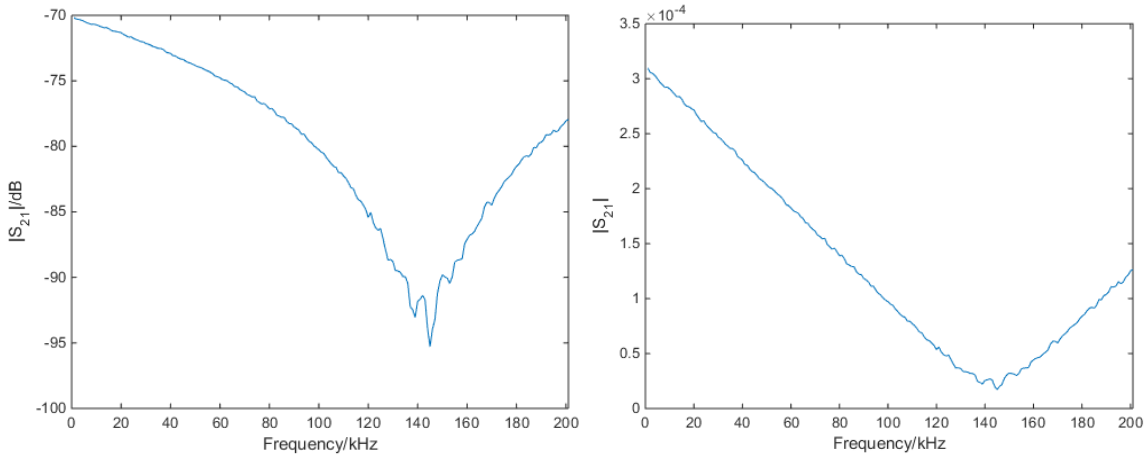

(a) (b)

Fig. 2.4 (a) A typical interferometer curve. (b) the absolute value curve.

errors could happen if we use software to get the minimum S parameter and its corresponding level from a large amount of measurement data. To avoid this error, a data fitting process in Matlab is applied to the absolute value curve to fit the two sides into two linear curves. The crossing point of the two curves indicates the frequency at which the minimum S parameter should happen. The data fitting process could effectively remove some noise and lower the S parameter level by around 10 dB compared to direct reading from the measured S parameter.

REFERENCES

[2.1] Vaughan, M. *The Fabry-Perot interferometer: history, theory, practice and applications.* CRC press, 1989.

[2.2] Hanssen, Ramon F. *Radar interferometry: data interpretation and error analysis.* Vol. 2. Springer Science & Business Media, 2001.

[2.3] Thompson, A. Richard, James M. Moran, and George W. Swenson Jr. *Interferometry and synthesis in radio astronomy.* John Wiley & Sons, 2008.

[2.4] Garrett, Michael A. "Radio Astronomy Transformed: Aperture Arrays-Past, Present & Future." *arXiv preprint arXiv:1211.6455* (2012).

[2.5] Rubiola, Enrico, and Vincent Giordano. "Advanced interferometric phase and amplitude noise measurements." *Review of Scientific Instruments* 73.6 (2002): 2445-2457.

[2.6] Nguyen, Cam, and Seoktae Kim. *Theory, Analysis and Design of RF Interferometric Sensors.* Springer Science & Business Media, 2011.

[2.7] Song, Chunrong, and Pingshan Wang. "A radio frequency device for measurement of minute dielectric property changes in microfluidic channels." *Applied Physics Letters* 94.2 (2009): 023901.

[2.8] Yang, Yang, et al. "Distinguishing the viability of a single yeast cell with an ultra-sensitive radio frequency sensor." *Lab on a Chip* 10.5 (2010): 553-555.

[2.9] He, Yuxi. "Fabrication and characterization of radio-frequency sensors for liquid material detection." (2013).

[2.10] Cui, Yan, and Pingshan Wang. "The Design and Operation of Ultra-Sensitive and Tunable Radio-Frequency Interferometers." (2014).

[2.11] Wessel, J., et al. "Contactless Investigations of Yeast Cell Cultivation in the 7 GHz and 240 GHz Ranges." *Journal of Physics: Conference Series.* Vol. 434. No. 1. IOP Publishing, 2013.

[2.12] Randus, Martin, and Karel Hoffmann. "A simple method for extreme impedances measurement-experimental testing." *ARFTG Microwave Measurement Symposium, 2008 72nd.* IEEE, 2008.

[2.13] Dargent, T., et al. "An interferometric scanning microwave microscope and calibration method for sub-fF microwave measurements." *Review of Scientific Instruments* 84.12 (2013): 123705.

[2.14] Shen, Chao, et al. "Engineering spectrum and dispersion with filters for high-sensitivity radio frequency detections." *Applied Physics Letters* 105.3 (2014): 032902.

[2.15] Mendis, Rajind, et al. "Terahertz microfluidic sensor based on a parallel-plate waveguide resonant cavity." *Applied Physics Letters* 95.17 (2009): 171113.

[2.16] Cui, Yan, Yuxi He, and Pingshan Wang. "A quadrature-based tunable radio-frequency sensor for the detection and analysis of aqueous solutions." (2014): 1-3.

[2.17] Cui, Yan, et al. "A simple, tunable, and highly sensitive radio-frequency sensor." *Applied physics letters* 103.6 (2013): 062906.

CHAPTER THREE

ANALYSIS OF SINGLE PARTICLE OVER CPW

In this chapter, we briefly introduce the development of microwave based cell and particle measurements. Then the efforts by our group in this field are presented. Fig. 3.1 (a) shows a measurement of single particle passing over a CPW and Fig. 3.1 (b) is a cross-section and it shows that that particle moves horizontally. The setup poses as a difficulty to current numerical simulation software due to mesh operations. In order to solve this problem, an analytical approach based on conformal mapping is presented in section 3.2 which provides a potentially effective way to solve this problem. Before that, the calculation procedure of the CPW field patterns is briefly described in 3.2.1, which is the fundamental of the calculation. In 3.3, the calculation in 3.2 is applied into microfluidic channel and the interferometer system for a complete application.

3.1 Introduction to RF Cell and Particle Measurement

Cell analysis with micro-fabricated systems becomes a hot research topic in the recent decade with the development of microfluidic [3.1] and microsystem technology [3.2] [3.3]. Micro-fabricated systems could provide cells with cues in a controllable and cost effective fashion that cannot be achieved by traditional approaches, and be easily linked to other detecting devices that probe the biomedical characters which governs cell behavior [3.4]. As for particles, many efforts are made for particle counting with microfluidic and microsystem technology [3.5].

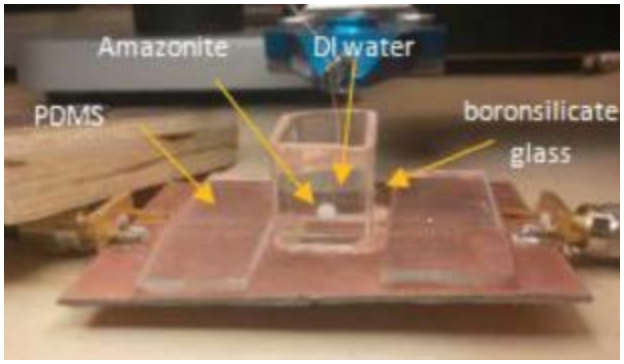

(a)

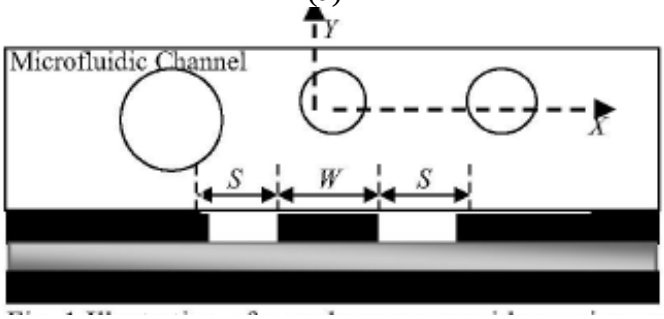

(b)

Fig. 3.1 (a) particle measurement with CPW (b) cross section of the CPW.

Among the sensing methods, microwave technique remains a promising approach due to its label-free and cost effective nature [3.6]. Compared to traditional methods, microwave techniques do not need the time-consuming procedures such as fluorescent tagging or cell staining. As an example, a microwave interdigital capacitor is fabricated and could differentiate live and dead cells in a broad band [3.7]. As an example of particle detection, a micro-fabricated CPW detector is devised and could detect a particle flow rate over $1.5*10^6$ beads per hour [3.8]. The device is applied for cell identification and sorting as well [3.9].

Our group has been working on measuring cells and particles with RF interferometer for several years. As mentioned in chapter 2, live and dead yeast cells

going through a microfluidic channel could be distinguished with an on chip interferometer [2.8]. Efforts have been made to distinguish normal and infected red cells as reported in [2.9]. Currently, projects on cell membrane heterogeneity and malaria cells measurements are undergoing by applying the microfluidic and microfabrication techniques into the RF interferometer system for potential high sensitivity applications.

3.2 S parameter When a Particle Passing over CPW

In order to find the S parameter when a particle passes over a CPW, we start from the field patterns of a CPW. The particle is divided into many cross sections along the signal line and the capacitance of each cross section is calculated separately. Then integration along the signal line is used to find the total S parameter.

3.2.1 The Field Patterns of Ground CPW

CPW is the main RF sensor we use among the uniform transmission lines since it has larger field intensity above the substrate [3.10]. Conformal mapping is the main analytical method to analyze a CPW since the very beginning [3.11]. The impedance, capacitance and effective permittivity of a CPW, including CPW, ground-CPW, with or without multiple dielectric layers, could be readily calculated. The equations are summarized in [3.12].

The basic procedure of analyzing CPW is to conformal map the electrical field lines starting from the signal line ending on the ground planes into parallel capacitors. In order to find the original field patterns, an inverse conformal mapping process from the

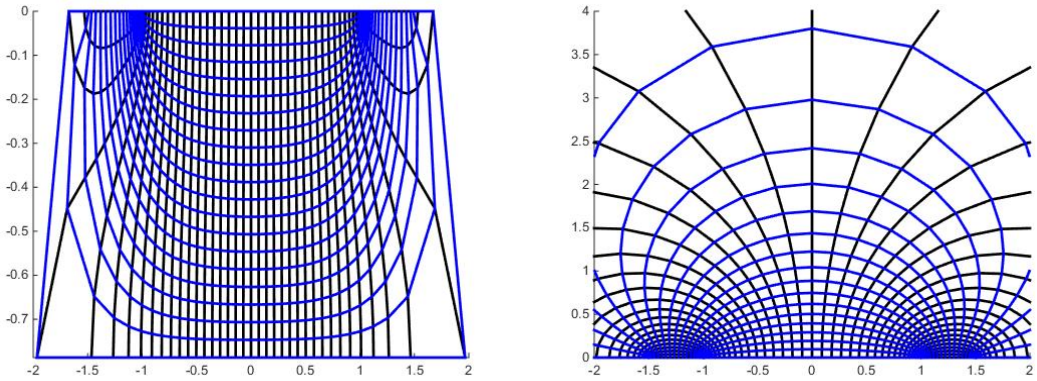

(a) (b)

Fig. 3.2 The field patterns (a) below and (b) above a ground-CPW (electrical fields are black lines and magnetic fields are blue lines).

parallel capacitor to CPW is used. The details are described in [3.13] [3.14]. The method divides the parallel capacitor into equal squares and then maps the square boundaries back to the CPW, which are the field patterns of the CPW, as shown in Fig. 3.2 (a) and (b): the signal line is from -1 to 1, the gaps lie in [-1.5, -1] and [1, 1.5], the two further ends are grounds. A magnetic wall is assumed at the substrate and air surface in the gaps. This method ensures that through each of the curvilinear squares the same power is transmitted.

3.2.2 Analysis Procedure of a Cell over CPW

Perturbation method is a technique used to solve a model in which a small material is introduced. It assumes that the actual fields of an RF device are not greatly different from those of the unperturbed if small pieces of dielectric or metallic materials

are introduced [3.15]. Thus, we assume that the field patterns are not altered by the presence of cells or particles, which are dimensionally small compared to the RF device.

To analyze a cell or particle over a CPW, we first divide the model into several cross-sections along the signal line direction. Capacitance is calculated along the signal line direction for each cross section. In the end, the results of all cross sections are integrated or summed to find the total effect caused by the presence of the cell or particle.

The first step is to find the capacitance per unit length of each cross section. With the field patterns we obtained in 3.2.1, we can simply find the grids occupied by the cell or particle in each cross section. Fig. 3.3 is the percentage of the grids occupied by a radius = 1 particle over the same CPW described in Fig. 3.2. For each pixel in the figure, the center of the particle lies exactly at the pixel. The plot shows effect of particle position on the signal of the transmission line. We can see from the plot that the particle has the most effect on the CPW when it is over the two edges of the signal line or right above the gap. At some heights, as the particle departs horizontally from the center, the phase change increases to the maximum at some position over the gap then decreases as the particle moves over the ground plane. This is observed in some measurements and is reported in [3.8] as well.

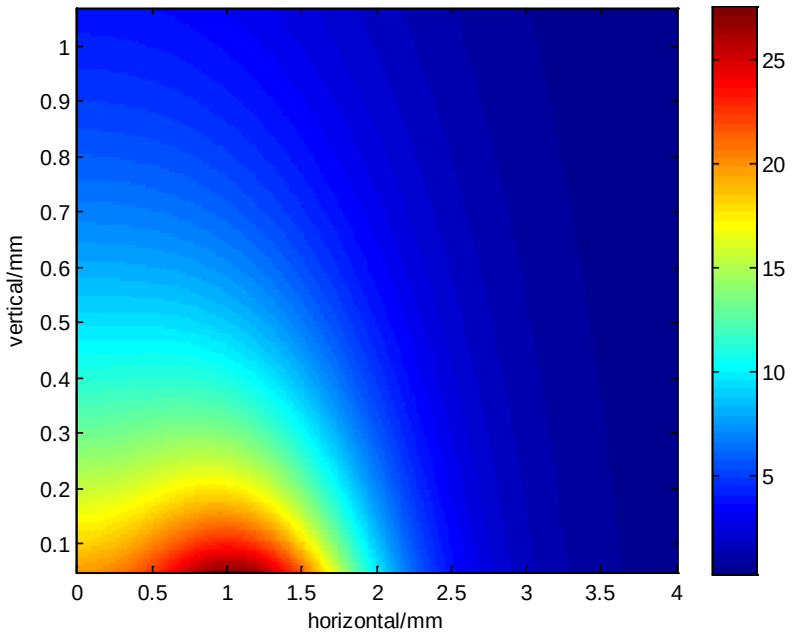

Fig. 3.3 Percentage of grids blocked by a circle with radius = 1 mm.

(3.1) is the universal equation for calculating the capacitance of a transmission line. From (3.1) we can see that the effective permittivity equals the mean permittivity above the CPW if the electrical field is unaltered by the particle of cell. Therefore the capacitance will be proportional to the effective permittivity

$$C = \frac{\varepsilon}{|V_0|^2} \int \bar{E} \cdot \bar{E}^* \, ds \tag{3.1}$$

If the background permittivity is ε_{eff0} and the permittivity with particle is ε_{eff}, the propagation constant is proportional to the square root of its capacitance as in (3.2)

$$\beta = \beta_0 \sqrt{\frac{\varepsilon_{eff}}{\varepsilon_{eff0}}} \tag{3.2}$$

We then integrate (or sum) β along the signal line to get the phase change caused by the particle. The sum arrives at the total electrical length difference caused by the particle as in (3.3).

$$\Delta\theta = \int_{-r}^{r}(\beta - \beta_0)\, dz = \beta_0 \Delta z \sum \left(\sqrt{\frac{\varepsilon_{eff}}{\varepsilon_{eff0}}} - 1 \right) \tag{3.3}$$

Using the mean permittivity might cause troubles since the traditional approaches of calculating capacitance are not as straightforward. We then tested another calculation method from the parallel capacitor perspective. The dielectric layer between the parallel plates is ε_r and there is a slab between the plates, whose permittivity is ε_{r1} and its thickness is qd while the total thickness of the capacitor is d. We have:

$$C = \frac{\varepsilon_0 \varepsilon_r A}{qd} \parallel \frac{\varepsilon_0 \varepsilon_r A}{(1-q)d} = \frac{\varepsilon_r}{(1-q)\varepsilon_r + q\varepsilon_{r1}} C_0 \tag{3.4}$$

From the EM field patterns of a CPW, we can map the grids occupied by the cell or particle back to the parallel capacitor, as in Fig. 3.4. The parallel capacitor is further divided into many capacitors in parallel. For each of them, the capacitance could be found with (3.4) and the total capacitance is the sum of all the capacitors. One concern was had that there might be reflections between the particle and the medium which is not considered here. However, reflection is not taken into account in publications when dealing with multilayer substrate CPW problems in the quasi-static analysis.

After finding the capacitance of each cross section, the effective permittivity and the impedance of each section can be readily calculated. Along the signal line, the impedance changes gradually. Below is the equation calculating reflection adapted from small reflections calculation [3.15] for the symmetrical case as in the particle model.

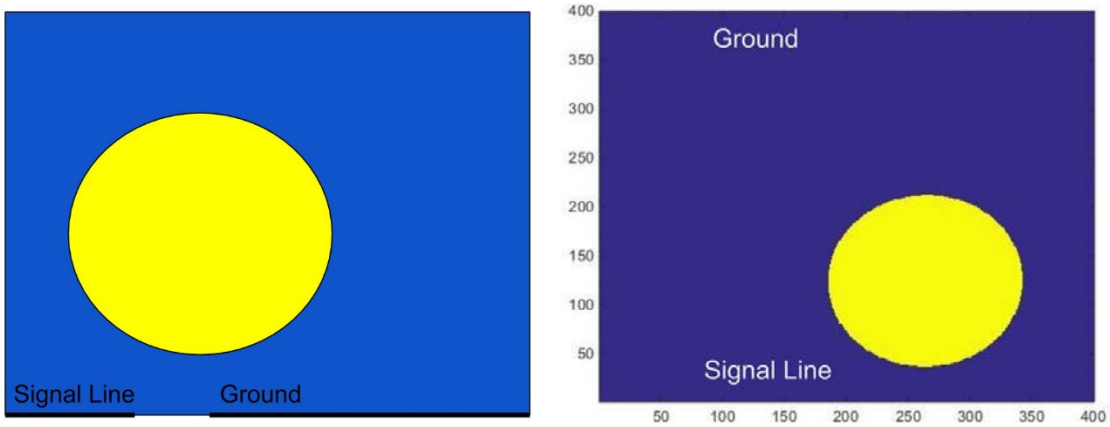

Fig. 3.4 Conformal mapping the CPW with particle to a parallel capacitor.

$$\begin{aligned}\Gamma(\theta) &= \Gamma_0 + \Gamma_1 e^{-2j\theta_1} \dots \Gamma_{N-1} e^{-2j(N-1)\theta_{N-1}} - \Gamma_{N-1} e^{-2jN\theta_{N-1}} \dots \Gamma_1 e^{-2j(2N-2)\theta_1} \\ &\quad - \Gamma_0 e^{-2j(2N-1)\theta_0} \\ &= e^{-j(2N-1)\theta_0}\left[\Gamma_0 e^{j(2N-1)\theta_0} - \Gamma_0 e^{-j(2N-1)\theta_0}\right] + \cdots \\ &\quad + e^{-j(2N-1)\theta_{N-1}}\left[\Gamma_{N-1} e^{j\theta_{N-1}} - \Gamma_{N-1} e^{-j\theta_{N-1}}\right] \\ &= 2je^{-j(2N-1)\theta_0}\Gamma_0 sin(2N-1)\theta_0 + \cdots + 2je^{-j(2N-1)\theta_{N-1}}\Gamma_{N-1} sin\theta_{N-1}\end{aligned} \tag{3.5}$$

3.3 S Parameter of the Liquid Covered Transmission Line

The cell or particle is conducted through a microfluidic channel which lies over the transmission line. The impedance of the uncovered transmission line is usually 50 Ohm, which we note as Z_0. According to the impedance calculation equations in [3.12], Z_0 will be altered to Z_1, usually decreasing to a value of tens of Ohms, if the transmission line is covered by dielectric liquid. The covered length is *l*. Due to the lossy characteristic at high frequency of the dielectric liquid, Z_1 is usually a complex number. The Z_0-Z_1-Z_0 structure has to be considered in the particle or cell analysis. The complex reflection seen

from the air, the transmission into the liquid and the transmission into the air from the liquid are as (3.6)

$$\Gamma = \frac{Z_1 - Z_0}{Z_0 + Z_1};\ T_1 = \frac{2Z_1}{Z_0 + Z_1};\ T_2 = \frac{2Z_0}{Z_0 + Z_1} \tag{3.6}$$

The total transmission and reflection coefficients can be calculated by summing the infinite bouncing waves with the reflection and transmission coefficients in (3.6). The results are validated in [3.16] which uses T matrix to arrive at the same result.

$$\boldsymbol{S}_{21} = T_1 T_2 e^{-\gamma l} + T_1 T_2 \Gamma^2 e^{-3\gamma l} + \cdots = \frac{1-\Gamma^2}{e^{\gamma l} - \Gamma^2 e^{-\gamma l}} = \frac{2Z_0 Z_1}{2Z_0 Z_1 cosh\gamma l + \left(Z_0^2 + Z_1^2\right) sinh\gamma l} \tag{3.7}$$

$$\boldsymbol{S}_{11} = \Gamma - T_1 T_2 \Gamma e^{-2\gamma l} - T_1 T_2 \Gamma e^{-2\gamma l} - \cdots = \frac{2\Gamma sinh\gamma l}{e^{\gamma l} - \Gamma^2 e^{-\gamma l}} = \frac{\left(Z_0^2 - Z_1^2\right) sinh\gamma l}{2Z_0 Z_1 cosh\gamma l + \left(Z_0^2 + Z_1^2\right) sinh\gamma l} \tag{3.8}$$

Many works have been done in this direct way of dielectric liquid measurement [3.16] [3.17]. From measured transmission and reflection parameters as in (3.7) and (3.8), we could have (3.9) from which we could find the complex propagation constant

$$\gamma l = cosh^{-1}\left(\frac{1 + S_{21}^2 - S_{11}^2}{2S_{21}}\right) \tag{3.9}$$

When a particle or cell passes over the transmission line in the microfluidic channel, the phase changes caused by the cell or particle as in (3.3) and (3.5) could be inserted into (3.7) and (3.8), which are the transmission and reflection coefficients of the sensor with particle and cell in the microfluidic channel. As for our interferometer, it is recommended to combine the discussion in this chapter with that in chapter II for a complete interferometer analysis.

Fig. 3.5 is an example of the analysis in Chapter II and III applied for a particle measurement. The millimeter plastic particle is moved horizontally at a certain height

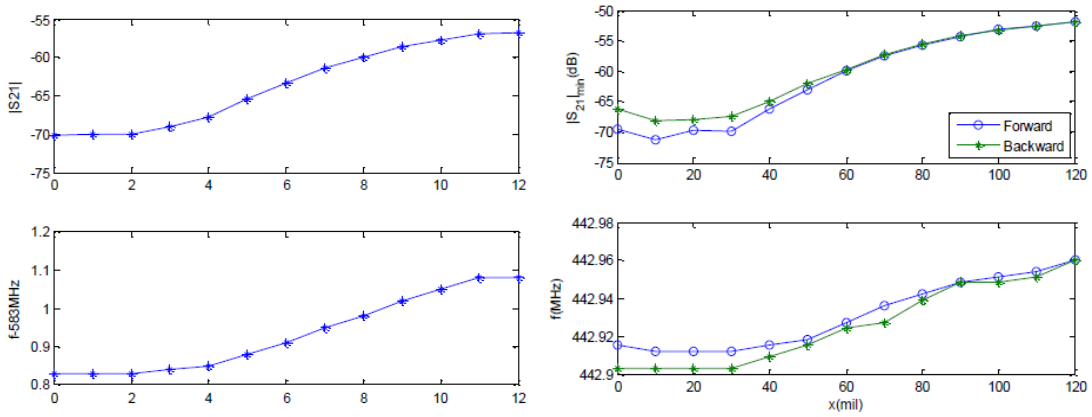

(a) (b)

Fig. 3.5 (a) calculated and (b) measured results of a particle measurement.

over the CPW in water with a micromanipulator at a step of 0.01". The analysis gives a same trend with the measurement results. There are some discrepancies, such as the frequency shift from analysis is around 0.3 MHz and that from measurement is 0.5 MHz. This is reasonable for the many factors that could not be included into the analysis such as the inevitable errors. From Fig. 3.5 we can see that the analysis in these two chapters could provide some insights into the RF interferometer.

REFERENCES

[3.1] Whitesides, George M. "The origins and the future of microfluidics." *Nature* 442.7101 (2006): 368-373.

[3.2] Yin, Huabing, and Damian Marshall. "Microfluidics for single cell analysis." *Current opinion in biotechnology* 23.1 (2012): 110-119.

[3.3] Qi, D., D. Hoelzle, and A. Rowat. "Probing single cells using flow in microfluidic devices." *The European Physical Journal-Special Topics* 204.1 (2012): 85-101.

[3.4] El-Ali, Jamil, Peter K. Sorger, and Klavs F. Jensen. "Cells on chips." *Nature* 442.7101 (2006): 403-411.

[3.5] Zhang, Hongpeng, et al. "Methods for counting particles in microfluidic applications." *Microfluidics and nanofluidics* 7.6 (2009): 739-749.

[3.6] Grenier, Katia, et al. "Recent advances in microwave-based dielectric spectroscopy at the cellular level for cancer investigations." *Microwave Theory and Techniques, IEEE Transactions on* 61.5 (2013): 2023-2030.

[3.7] Chen, Tong, et al. "Broadband discrimination of living and dead lymphoma cells with a microwave interdigitated capacitor." Biomedical Wireless Technologies, Networks, and Sensing Systems (BioWireleSS), *2013 IEEE Topical Conference on. IEEE*, 2013.

[3.8] Wood, D. K., et al. "High-bandwidth radio frequency Coulter counter." *Applied Physics Letters* 87.18 (2005): 184106.

[3.9] Wood, D. K., et al. "A feasible approach to all-electronic digital labeling and readout for cell identification." *Lab on a Chip* 7.4 (2007): 469-474.

[3.10] Song, Chunrong, James E. Harriss, and Pingshan Wang. "Compensating on-chip transmission line losses for a high-sensitivity microwave sensor." *Sensors and Actuators A: Physical* 154.1 (2009): 7-11.

[3.11] Wen, Cheng P. "Coplanar waveguide: A surface strip transmission line suitable for nonreciprocal gyromagnetic device applications." *Microwave Theory and Techniques, IEEE Transactions on* 17.12 (1969): 1087-1090.

[3.12] Simons, Rainee N. *Coplanar waveguide circuits, components, and systems*. Vol. 165. John Wiley & Sons, 2004.

[3.13] Gillick, Matthew, Ian D. Robertson, and Jai S. Joshi. "An analytical method for direct calculation of E and H-field patterns of conductor-backed coplanar waveguides." *Microwave Theory and Techniques, IEEE Transactions on* 41.9 (1993): 1606-1610.

[3.14] Shao-jun, Fang, and Bai-Suo Wang. "Analysis of asymmetric coplanar waveguide with conductor backing." *Microwave Theory and Techniques, IEEE Transactions* on 47.2 (1999): 238-240.

[3.15] Pozar, David M. *Microwave engineering*. John Wiley & Sons, 2009.

[3.16] Barry, Walter. "A broad-band, automated, strip line technique for the simultaneous measurement of complex permittivity and permeability." *Microwave Theory and Techniques, IEEE Transactions on* 34.1 (1986): 80-84.

[3.17] Booth, James C., et al. "Quantitative permittivity measurements of nanoliter liquid volumes in microfluidic channels to 40 GHz." *Instrumentation and Measurement, IEEE Transactions on* 59.12 (2010): 3279-3288.

CHAPTER FOUR

EXPLOITING FILTER STOPBAND FOR RF INTERFEROMETER OPERATION

In this chapter, we evaluate the sensitivity enhancement of filters to the RF interferometer. We also propose to exploit filter stop band for high sensitivity RF interferometer operation by utilizing reflection scattering parameters. Combined with the pass band filter operation, the modified RF interferometer effectively expands its frequency coverage. The model in Section II is applied to analyze and predict interferometer performance. A high pass filter (HPF) and a low pass filter (LPF) are designed and built to demonstrate the interferometer operation as well as to verify the model over a frequency range of 1-4 GHz. Lossy materials are shown to degrade filter sensitivity enhancement effects significantly due to reduced group delay and lower RF fields. Further work is needed to address the issue.

4.1 Introduction

Among the many microwave measurement techniques, including direct scattering parameter measurement [4.1] and high quality factor resonator method [4.2], RF interferometers have demonstrated the highest sensitivity and broadband frequency tunability with convenient system design and operation flexibility [2.10]. Planar transmission lines, e.g. coplanar waveguides and micro strip lines, have been used in previous interferometers. Yet, the high sensitivity operation often requires a large stable dynamic range, such as ~130 dB, for minute signal detection. Thus, sophisticated

detection circuits are needed and the application of the interferometer in rugged environments is limited. To address this problem, filters and resonators are proposed to replace uniform transmission lines and enhance the interactions between the RF fields and material-under-test (MUT). Thus, MUT signals are boosted considerably and the required dynamic range is effectively reduced. The slowed probing wave velocity and enhanced local field intensity, when compared with that of uniform transmission line, are responsible for the improvement [2.14] [4.3].

However, only the pass band of the filters and resonators are utilized since the use of transmission scattering parameters requires reasonable $|\boldsymbol{S}_{21}|$. Thus, the achievable frequency coverage, i.e. the measuring of frequency dependent MUT information, is limited to the pass-band of the filters and resonators. In this chapter, we propose and demonstrate that the stop band of the filters can also be exploited for high sensitivity interferometer operations, together with the use of their pass-band properties.

Measuring minute property change of lossy material at high sensitivity is an important issue since biological and chemical MUTs are often lossy. For transmission line interferometers, losses, such as DI water for DNA solutions, do not cause appreciable sensitivity degradation since the system can be rebalanced with attenuators [4.4]. For resonators, the quality factors will drop significantly due to lossy MUT [4.5]. Thus interferometer sensitivity enhancement will also be reduced. For filters, lossy material effects on their dispersion and wave velocity as well as techniques to compensate loss effects are active research topics [4.6]. Thus, we investigate the effects of lossy material on filter performance for interferometer sensitivity enhancement.

To study the above mentioned issues, we design two compact CPW-based filters, one LPF and one HPF. We also apply the mathematical model in Section II to predict the sensitivity of the interferometers based on the broadband properties of the sensing elements. The model is used to retrieve MUT property from measurement results as well.

4.2 The Design of the Filters

An LPF as in Fig. 4.1(a) and an HPF as in Fig. 4.1(c) are designed in HFSS and ADS and fabricated with a milling machine on a Duroid 5870 laminate to investigate the use of $\boldsymbol{S}_{11}$ in conjunction with $\boldsymbol{S}_{21}$ for MUT sensing. A reasonable transmission coefficient in pass band with longer group delay τ_d and stronger local fields are the main filter design considerations. CPW structure is used to build the filters since it is compact, simple and uniplanar with smooth transitions for convenient fabrication and testing. A pass band between 2 and 3 GHz is selected. The pass-band together with its adjacent stop band used for $|\boldsymbol{S}_{11}|_{min}$ measurement is within the operating frequency of our available circuit components. A CPW is built for sensitivity comparison. The total physical length and width, signal line and gap width of the filters and the comparison CPW are the same as depicted in Fig. 4.1(a) (c). Polydimethylsiloxane (PDMS) is used as MUT.

The LPF is comprised of two back-to-back short-end CPW series stubs [4.7]. In Fig. 4.1(a), L_f = 19 mm and W_f = G_f = 0.4 mm. Its equivalent circuit in Fig. 4.1(b) is a simplified model originated from [4.7] neglecting capacitors between the narrower signal lines and the branched arms: L_1 = 4.46 nH, L_2 = 0.06 nH, C_1 = 1.31 pF. The element values are obtained through parameter fitting. The HPF contains two shunt inductors (no

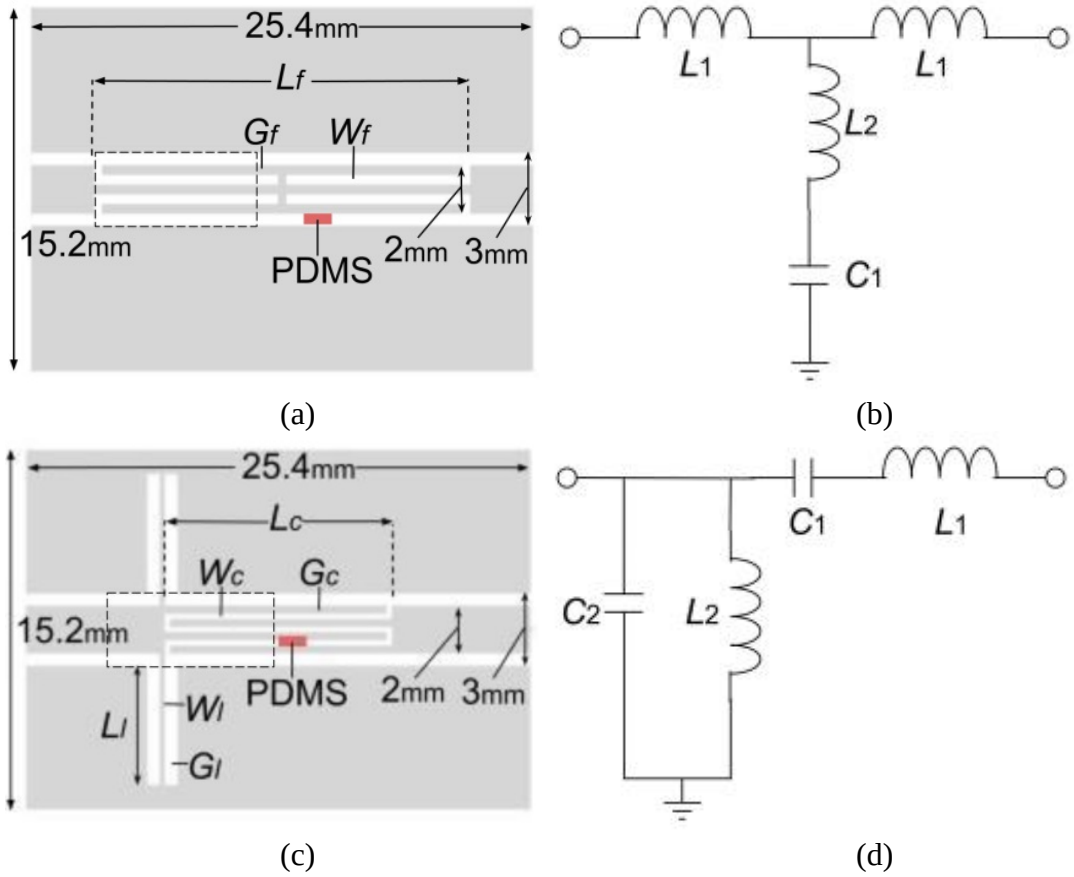

Fig. 4.1 (a) Layout of the LPF. (b) An equivalent circuit model of the LPF. (c) Layout of the HPF. (d) An equivalent circuit model of the HPF.

air bridge) and a series interdigitated capacitor (IDC) as in Fig. 4.1(c): L_c = 11.4 mm, G_c = 0.2 mm, W_c = 0.36 mm, L_l = 5.6 mm, G_l = 0.64 mm, W_l = 0.25 mm. Its circuit model is in Fig. 4.1(d): L_1 = 1.1 nH, C_1 = 0.9 pF, L_2 = 1.65 nH, C_2 = 0.7 pF. It is similar to one cell of the composite right hand transmission line metamaterial [4.8] and it is expected to have a negative propagation coefficient. The IDC value C_1 and the shunt inductor L_2 are extracted from ADS. The parasitic series inductance L_1 and the shunt capacitor C_2 are obtained from parameter fitting to fit the circuit response curve to that of simulated one.

The transmission coefficients of the filters and the CPW are shown in Fig. 4.2(a). The results from the equivalent circuit modeling, full wave simulations shown as dashed lines and measurements shown as solid lines agree with each other reasonably well. The filters enable the interferometer to operate with $\boldsymbol{S}_{21}$ between 2 and 3 GHz. Higher insertion loss will affect $\boldsymbol{S}_{21}$ sensitivity. The group delay diagram, both measured (solid lines) and simulated (dashed lines), in Fig. 4.2(b), shows that the LPF has slow waves, mainly due to the large inductance from the reduced center conductor width. The discrepancy of the HPF delay is due to the dropping as shown in Fig. 4.1(a). Simulation shows approximately 2 times larger $|\boldsymbol{E}_{rf}|$ at MUT position in Fig. 4.1(a) near the cut-off frequency f_c compared to the field of the CPW. For the HPF, it has around 4 times larger group delay and the coupling IDC creates around 5 times larger $|\boldsymbol{E}_{rf}|$ in the interdigitated gaps near f_c. Therefore, the filters are expected to achieve stronger RF-MUT interactions than the CPW due to the longer interaction time τ_d and stronger field intensity in the $\boldsymbol{S}_{21}$ measurement. Fig. 4.2(c) shows $|\boldsymbol{S}_{11}|$ of the filters. As expected, reflections in the stop bands are strong. Their group delays, as in Fig. 4.2(d), are smaller than the delay of transmission in pass band. The field distribution in stop-band of the filters shows a greater intensity at the filter and transmission line junction than in the pass-band. Thus, we put MUT at these junction positions in $\boldsymbol{S}_{11}$ measurements. Based on the above observations, we expect the $\boldsymbol{S}_{11}$ and $\boldsymbol{S}_{21}$ operations have similar sensitivities.

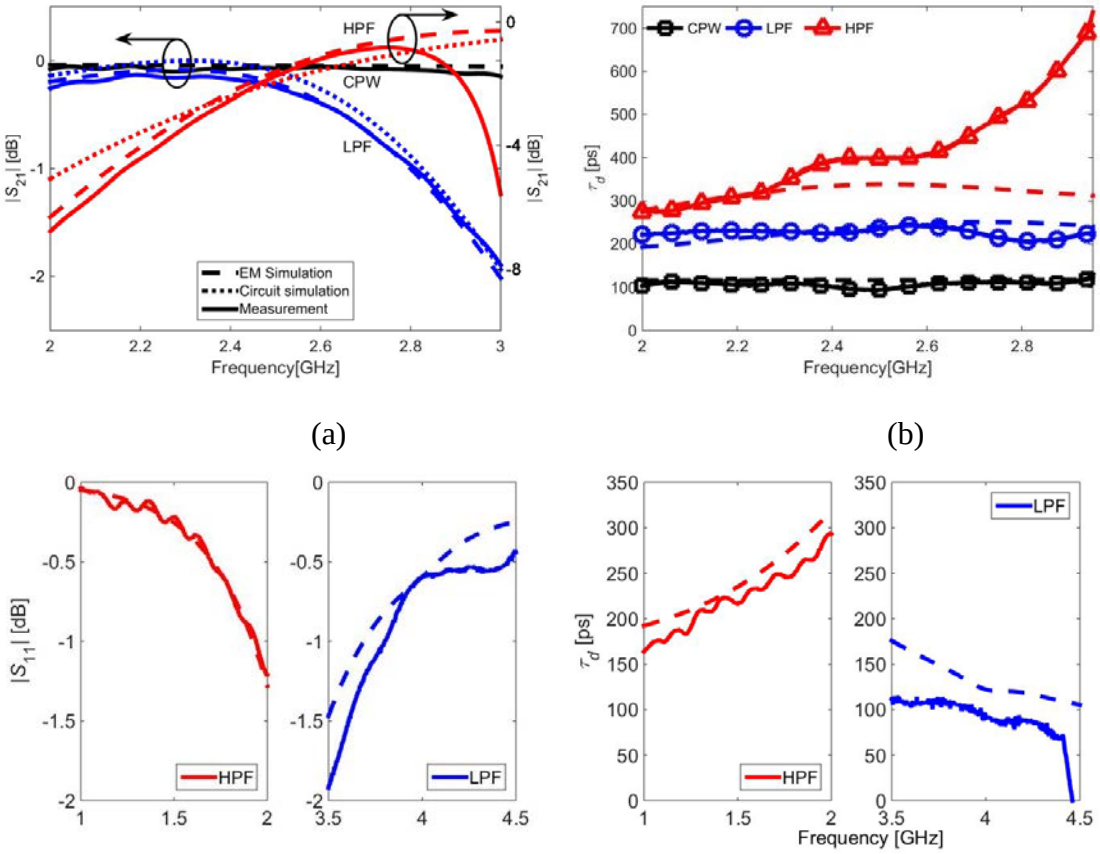

Fig. 4.2 (a)(b) $|\boldsymbol{S}_{21}|$ and transmission delay of the CPW and the filters in pass band. (c)(d) $|\boldsymbol{S}_{11}|$ and reflection delay of the filters in stop band.

4.3 Interferometer Operations

The obtained filters and CPW are incorporated into the system in Fig. 2.1 to investigate interferometer performance. A small PDMS sample (2mm ×0.5mm ×0.5mm) is used as dielectric MUT and placed at where $|\boldsymbol{E}_{rf}|$ is the strongest, such as the locations indicated in Fig. 4.1.

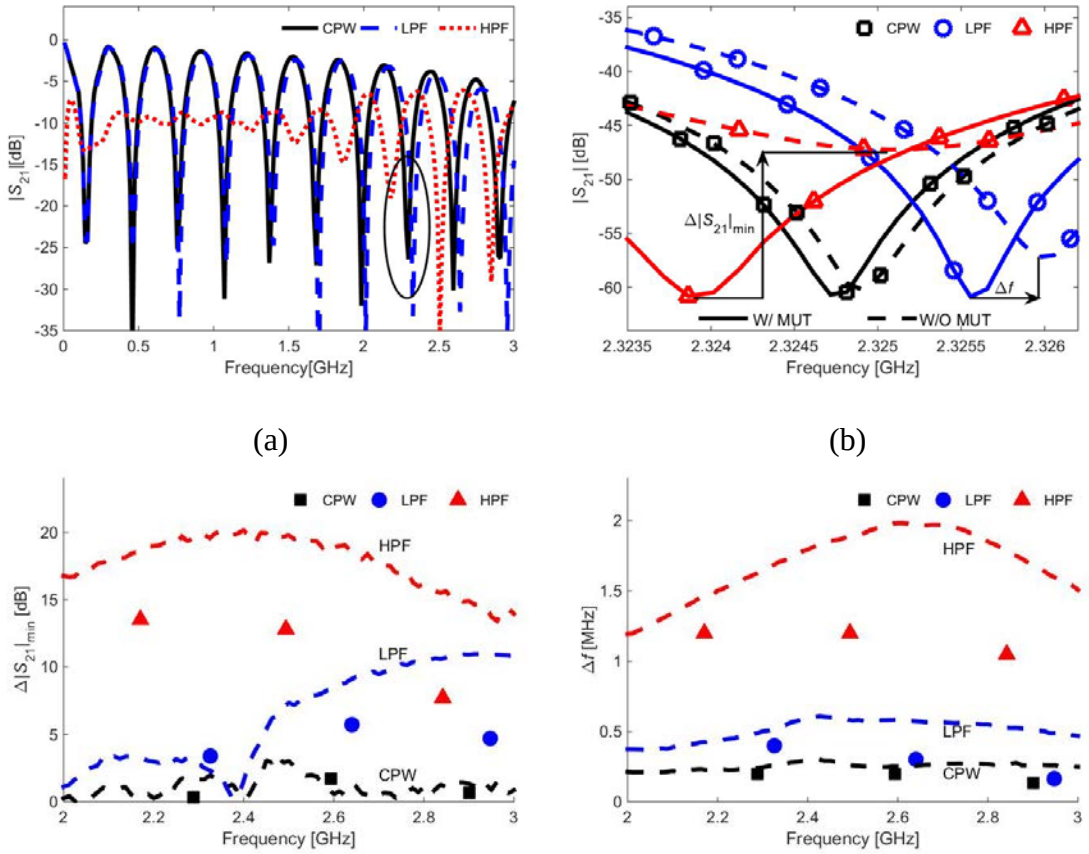

Fig. 4.3. Measurement results. (a) Broadband interferometer operation. (b) A zoom-in view of the 8th minima. (c) Measured and calculated $\Delta|\boldsymbol{S}_{21}|_{min}$, and (d) Δf of the interferometers.

4.3.1 Sensitivity Enhancement Test: Measuring $\boldsymbol{S}_{21}$

For convenience, we choose Φ so that the 8th to 10th minima of CPW and LPF based interferometers lie between 2 and 3 GHz, as shown in Fig. 4.3(a). Only one CPW and one LPF are used in MUT branch of Fig. 2.1 for CPW and LPF measurements. For HPF, the minima numbers are difficult to recognize due to large insertion loss at low frequencies. One HPF is used in each branch to cancel out the non-zero phase at DC for

simplicity in analysis. At each harmonic, R_1 and R_2 in Fig. 1 are tuned to achieve a $|\boldsymbol{S}_{21}|_{min}$ of -60 dB, as shown by the solid lines in Fig. 4.3(b) for the 8th minima. The system is stable and reliable for investigation at the level of -60 dB. The MUT is then introduced to shift the curves to the dashed lines in Fig. 4.3(b). In Fig. 4.3(b), the CPW and HPF plots have been shifted 36.3 and 153.4 MHz higher, respectively, relative to their original value in (a) for clearer comparison. Fig. 4.3(c)-(d) show the measured $\Delta|\boldsymbol{S}_{21}|_{min}$ and Δf at three frequencies. It is shown that the HPF enables the highest sensitivity in both $\Delta|\boldsymbol{S}_{21}|_{min}$ and Δf followed by LPF. The Δf trend agrees with the group delay qualitatively. The $\Delta|\boldsymbol{S}_{21}|_{min}$ of filters are much larger than that of CPW due to stronger interactions between the PDMS slab and RF fields despite their higher insertion loss.

The dashed lines in Fig. 4.3(c) and (d) are calculated results with the equations described in section II. Broadband measurement results of the filters and comparison CPW are used for calculation. The calculated results are also validated by simulations at frequencies around the symbols by importing broadband filter measurement results, with and without MUT, into a circuit model of the interferometer in Fig. 2.1. The predictions of measured sensitivity from calculation are reasonable even though the measured results are significantly lower. A possible reason for the discrepancy is that the frequency dependent properties of actual circuit components are not considered in calculation and simulations.

To obtain the permittivity from the measured scattering parameters of a given MUT at a given MUT location, we use (2.5)-(2.7). First, $\Delta\Phi_F$, which is the phase change of the interferometer caused by MUT, is obtained with (2.7) and the measured Δf in Fig.

TABLE 4.1

Calculated MUT permittivity from interferometer measured results

Sensor Type	1	2	3
CPW	3.0921	2.8600	2.1223
LPF	3.0494	2.4137	1.9445
HPF	2.4884	2.3195	2.4582

4.3(d). The magnitude information is not used here since the components in the system shows magnitude variation as frequency shifts. Then, parametric simulations in HFSS are conducted for the comparison CPW and filters to provide a relationship between $\Delta\Phi_F$ and the permittivity of the MUT. Compare the results from the two steps, MUT permittivity is obtained, similar to the process in [4.9]. The calculated results are shown in Table 4.1 for the 3 frequencies in Fig. 4.3(d) as 1-3.

The calculated ε_r ranges between 2 and 3, which is the often reported permittivity of PDMS. The HPF and the two higher frequency points of LPF give smaller permittivity values, which are also indicated in the calculated results (frequency shifts) in Fig. 4.3(d) since the measured results are smaller than the calculated ones. The deviation is believed to be caused in part by the uncertainty of MUT locations in Fig. 4.2.

4.3.2 Fundamental mode operation: higher sensitivity

We modified the branch length of the interferometer to satisfy $n = 1$ at 2.35, 2.65 and 2.95 GHz respectively for the filter and CPW based system operation. The filters and

CPW are the same as in previous experiments with only different cables. Fig. 4.4 shows that the filters yield larger Δf and $\Delta|\boldsymbol{S}_{21}|_{\min}$ than those in Figs. 4.3 (c) and (d), which also agree reasonably well with the calculated results, i.e. fundamental frequency operation produces close to $(2n\text{-}1)$ times larger Δf. The $\Delta|\boldsymbol{S}_{21}|_{min}$ parameter is larger than the results in Fig. 4.3 since the frequency dependent transmission coefficient contribute to the larger amplitude change.

When an HPF is used in MUT branch while a CPW is used in REF branch, the results around 2.96 GHz are shown in Fig. 4.5. Smaller HPF Δf is obtained compared with the results in Fig. 4.4(b). There are a few possible reasons for the observed lower sensitivity. First, the HPF induces additional phase delay, i.e. Φ_0 in eq. (1), compared with CPWs. The delay makes the equivalent branch length longer. As a result, the interferometer may be working at higher harmonics mode at the targeted frequency. Another reason is that the frequency dependent A_1 ignored in section II makes the interferometer work with a different mechanism from the analysis in II. For ease of analysis, we assume that A_2 and Φ are frequency independent and $\Phi = \pi+\delta\varphi$ when MUT is induced. It can be shown that $|\boldsymbol{S}_{21}|_{min}$ happens at $A_1 = A_2\cos\Phi$ and $|\boldsymbol{S}_{21}|_{min} = |A_1\sin\delta\varphi|$. In this case, $\delta\varphi$ causes $|\boldsymbol{S}_{21}|_{min}$ to shift vertically other than horizontally.

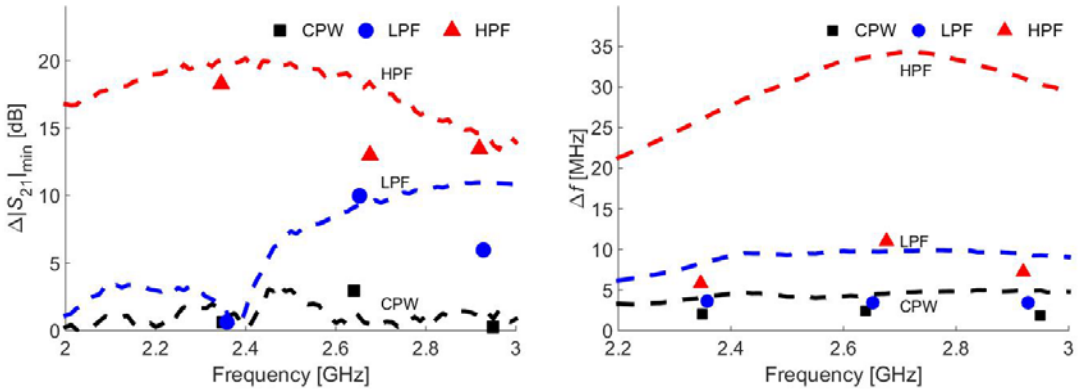

(a) (b)

Fig. 4.4. Measured sensitivity at n = 1 of the interferometer. (a) $\Delta|\boldsymbol{S}_{21}|_{min}$, with calculated $\Delta|\boldsymbol{S}_{21}|_{min}$ caused by MUT. (b) Δf with calculated results.

4.3.3 Lossy Materials

Dielectric measurements are often carried out with the presence of lossy material, such as DNAs in lossy buffer solutions [4.4]. The lossy buffer may alter the dispersion relationship of the filters and reduce their sensitivity enhancement effects. To investigate lossy material effects, an absorbing material of 3mm × 3mm × 9.5mm (MT-30, Cumming Microwave) is placed on the sensing structure surface along the signal line direction, as indicated by the dashed rectangle in Fig. 4.1. It covers the two CPW gaps of the CPW. Fig. 4.5 (a) and (b) show the measured broadband transmission coefficients and the delay of the filters before and after introducing the lossy material. For the HPF, the transmission coefficient almost stays the same since the permittivity of the lossy material shifts the curve left. The electrical field intensity decreases after the lossy material is introduced on filters and CPW. The delay of the filters is deteriorated when loss is introduced. Thus, loss of sensitivity for filters based interferometers is expected.

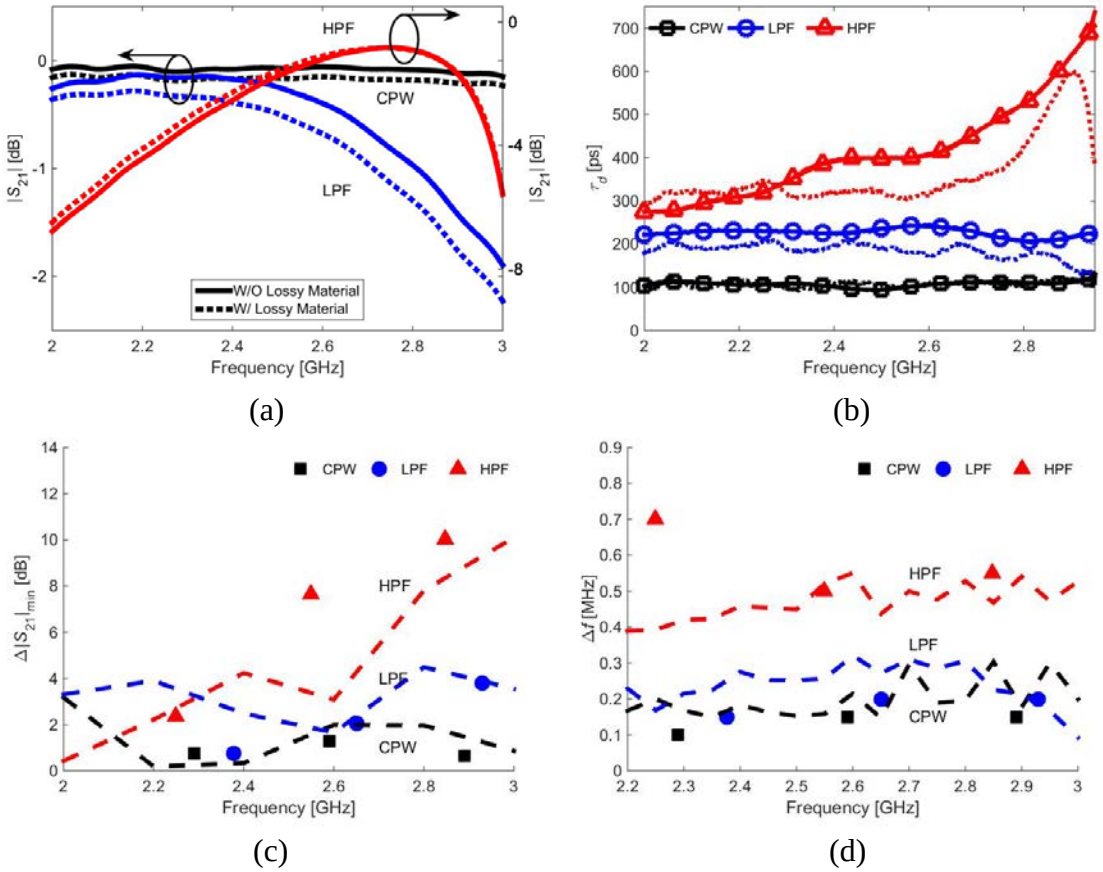

Fig. 4.5 Measurement results with lossy materials. (a)(b) $|\boldsymbol{S}_{21}|$ and delay of the CPW and the filters (c) (d) Measured and calculated $\Delta|\boldsymbol{S}_{21}|_{min}$ and Δf of the interferometer with lossy material.

TABLE 4.2
Calculated MUT permittivity with lossy material

Sensor type	1	2	3
CPW	2.5029	2.7460	3.0336
LPF	2.4157	2.6680	2.5721
HPF	2.7063	2.4053	3.0350

The interferometers are then tuned to -60 dB with the lossy material on the filters

and the CPW. The dielectric MUT is still placed where the electrical field is the strongest as in the measurements for sensitivity analysis above. The results are summarized in Figs. 4.5 (c) and (d). For both $\Delta|\boldsymbol{S}_{21}|_{min}$ and Δf, CPW has minimum degradation while filters experience more than twice Δf degradation due to loss effect. Δf degeneration trend is in agreement with the conclusions that group delay drops more significantly around cut-off frequency for filters and Δf is directly related to group delay. For $\Delta|\boldsymbol{S}_{21}|_{min}$, filters drop by half and CPW retains the same level. The calculated permittivity from each Δf are listed in Table 4.2. Loss effect on resonator is also evaluated with the resonator designed in [4.3]. Simulation and measurement results show that loss has similar effects on resonator and filters. Nevertheless, filters and resonators can still enhance interferometer sensitivity significantly when compared to CPWs.

4.4 Sensitivity Enhancement Test: Measuring S11

The setup in Fig. 2.1 allows the tuning of $\boldsymbol{S}_{11}$ in stop-band of the filters. Fig. 4.6(a) is the broadband performance of the interferometer between 2 and 4 GHz with an LPF in each branch. Fig. 4.6(b) is a zoom in view at ~2.55 GHz after tuning both $\boldsymbol{S}_{11}$ and $\boldsymbol{S}_{21}$ to ~ -60 dB. The *S* parameter starting levels, i.e. $|\boldsymbol{S}_{11,0}|$ and $|\boldsymbol{S}_{21,0}|$ in Fig. 4.1, of the interferometer follow the broadband $|\boldsymbol{S}_{11}|$ and $|\boldsymbol{S}_{21}|$ trend of LPF, respectively.

$\boldsymbol{S}_{11}$ and $\boldsymbol{S}_{21}$ can be tuned simultaneously at the same frequency point or different frequencies, such as Figs. 4.7(b)(c). However, for high sensitivity operation, it is easier to tune $\boldsymbol{S}_{11}$ and $\boldsymbol{S}_{21}$ separately, using one at a time. Therefore, in measurements below, we only tune $\boldsymbol{S}_{11}$ in stop-band with the same interferometer setup used for Fig. 4.4. A filter is

used in each branch to provide sufficient reflection for proper operation.

The results of $\Delta|\boldsymbol{S}_{11}|_{min}$ and Δf are summarized in Figs. 4.6(d) and (e). It is shown that $\Delta|\boldsymbol{S}_{11}|_{min}$ is on the same order with $\Delta|\boldsymbol{S}_{21}|_{min}$, but Δf is only half the values of $\boldsymbol{S}_{21}$ measurements. This is reasonable since the reflection wave travel distance doubles, and the frequency sensitivity is degraded according to previous analysis. These results show that the use of $\boldsymbol{S}_{11}$ effectively expands the working frequency to stop-band and is potential for high sensitivity measurement due to the strong field intensity.

The use of $\boldsymbol{S}_{11}$ is also attempted with CPW based interferometers. But the obtained results do not show reliable and repeatable trend. Much weaker reflections, since there is no stop-band, could be the main reason.

Quadrature hybrids were used to replace power dividers to obtain $\boldsymbol{S}_{11}$ information at the same operating frequency in [2.16]. No tuning was considered to achieve high sensitivity $\boldsymbol{S}_{11}$ operation. When such hybrids are used in Fig. 2.1 to replace the power dividers, the reflection signals can also appear at the input port of the left hybrid.

In summary, the interferometer architecture is modified to allow the tuning of $\boldsymbol{S}_{11}$. Thus, the working frequency bandwidth is expanded to include the stop-band. It is shown that the interferometer has similar sensitivity in stop-band as in pass-band. Thus, six-port circuit reflectometers could be exploited to build on chip interferometer system with the circuit in Fig. 2.1 [4.16]. Furthermore, the proposed model predicts the sensitivity of the interferometer reasonably well. Nevertheless, lossy materials degrade sensitivity enhancement effects of filters and resonators due to reduced group delay. Further work is needed to overcome this issue.

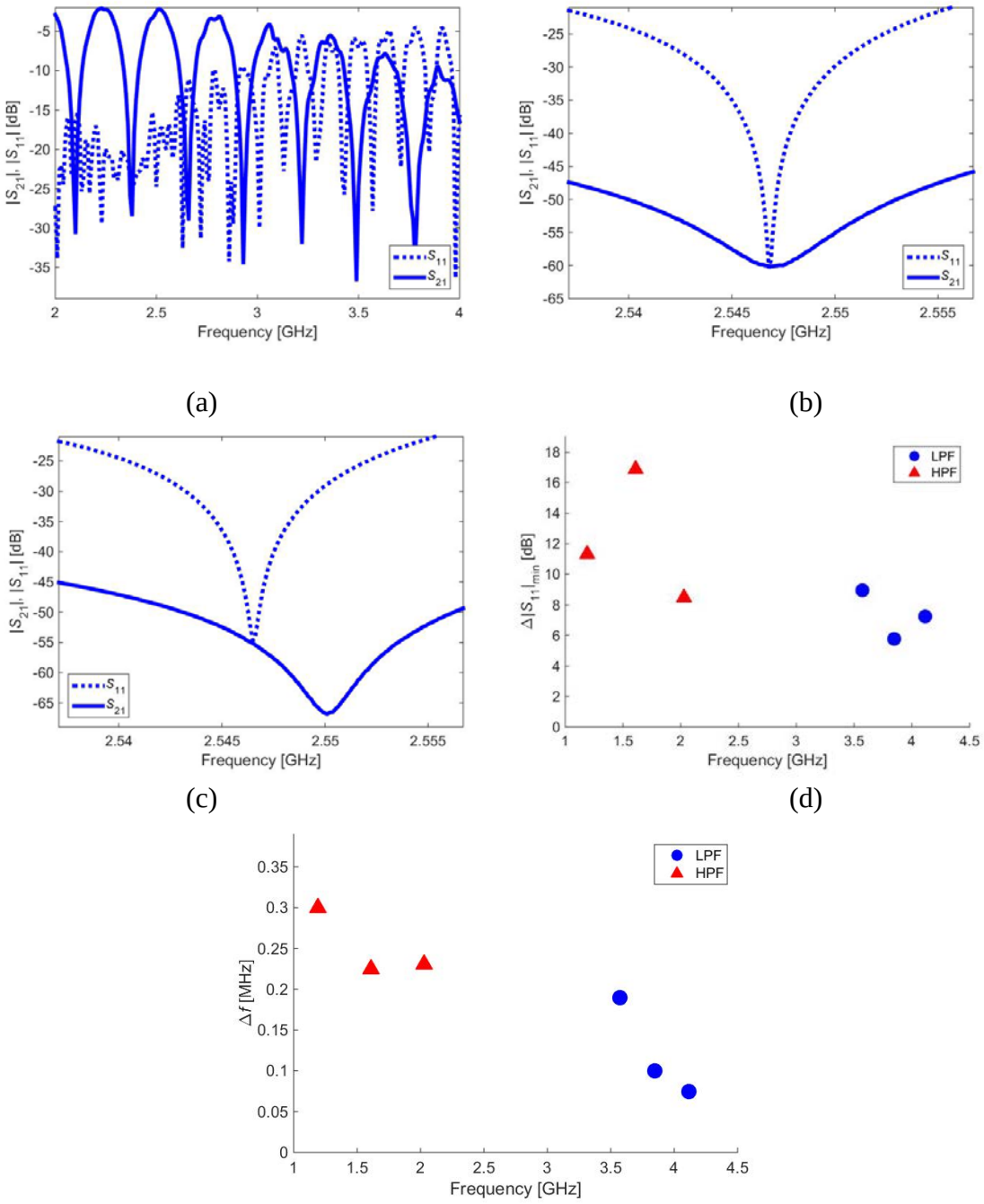

Fig. 4.6 (a) Broadband interferometer operation with LPF measuring $\boldsymbol{S}_{11}$ and $\boldsymbol{S}_{21}$ at the same time. (b)(c) A zoom-in view at ~2.55 GHz measuring $\boldsymbol{S}_{11}$ and $\boldsymbol{S}_{21}$ at the same time. (d) Measured $\Delta|\boldsymbol{S}_{11}|_{min}$ and (e) Δf of $\boldsymbol{S}_{11}$.

REFERENCES

[4.1] Hofmann, Maximilian, et al. "Microwave-based noninvasive concentration measurements for biomedical applications." *IEEE Trans. Microw. Theory Techn.*, 61.5 (2013): 2195-2204.

[4.2] Lee, Hee-Jo, Kyung-A. Hyun, and Hyo-Il Jung. "A high-Q resonator using biocompatible materials at microwave frequencies." *Applied Physics Letters* 104.2 (2014): 023509.

[4.3] Chen, Zhe, Yongzhi Shao, and Pingshan Wang. "Resonator and Filter Induced Slow Waves for High-Sensitivity RF Interferometer Operations." (2014).

[4.4] Cui, Yan, et al. "Highly sensitive RF detection and analysis of DNA solutions." Microwave Symposium (IMS), *2014 IEEE MTT-S International*. IEEE, 2014.

[4.5] Gregory, Andrew P., and Robert N. Clarke. "A review of RF and microwave techniques for dielectric measurements on polar liquids." *IEEE Trans. Dielec. Elec. Insu.*,13.4 (2006): 727-743.

[4.6] Tsai, Chih-Ming, and Hong-Ming Lee. "The effects of component Q distribution on microwave filters." *IEEE Trans. Microw. Theory Techn.*, 54.4 (2006): 1545-1553.

[4.7] Sor, James, Yongxi Qian, and Tatsuo Itoh. "Miniature low-loss CPW periodic structures for filter applications." *IEEE Trans. Microw. Theory Techn.*, 49.12 (2001): 2336-2341.

[4.8] L. Anthony, T. Itoh, and C. Caloz. "Composite right/left-handed transmission line metamaterials." *Microwave Magazine, IEEE* 5.3 (2004): 34-50.

[4.9] Chretiennot, Thomas, David Dubuc, and Katia Grenier. "A microwave and microfluidic planar resonator for efficient and accurate complex permittivity characterization of aqueous solutions." *IEEE Trans. Microw. Theory Techn.*, 61.2 (2013): 972-978.

[4.10] Li, Chaojiang, Hanqiao Zhang, and Pingshan Wang. "A novel six-port circuit based on four quadrature hybrids." International Journal of RF and Microwave Computer-Aided Engineering 20.1 (2010): 128-132.

CHAPTER FIVE

RF INTERFEROMETER FOR VOLATILE ORGANIC COMPONENTS DETECTION

In this chapter, an application of the RF interferometer measuring volatile organic component (VOC) is described. Micrometer sensors are designed, fabricated and incorporated into the RF interferometer to test the *S* parameter response after certain concentration VOC gas is introduced to the surface of the sensors. The sensors are coated with PGMA polymer and a gas dilution system is built to give exact concentration gas. Preliminary results show that the RF interferometer could response effectively to VOC and further work is needed to decrease the limit of detection.

5.1 Introduction

An urgent need for reliable and quick detection of chemical warfare agents (CWA) and toxic industrial chemicals (TIC) is on the rise due to the increasing threaten of CWA and TIC to public safety. Many detection methods have been intensively explored, such as the traditional gas chromatography, laser spectroscopy and acoustic wave sensors [5.1] [5.2]. Electrical method detecting VOC are developed as well, such as the chemical sensitive capacitors [5.3] [5.4]. Electrical approach in the RF frequency bandwidth is a relatively new method being investigated in recent years [5.5] [5.6] [5.7]. The previous work demonstrates the potential advantages of high sensitivity, real time response, low cost and portability of VOC detection with RF approach. To this end, the primary objective of this work is to evaluate the RF interferometer method exploiting RF

sensor coated with specific polymer for application of highly sensitive, selective, near real-time (NRT) monitoring of CWAs and TICs.

The RF interferometer has been proven highly sensitivity in terms of dielectric changes detection while chemo-selective polymers provide the fundamentals of detection and selectivity. A vapor dilution system is developed and built to achieve low concentration vapor with high accuracy. Micrometer sensing transmission lines (TL) are designed and fabricated to improve the sensitivity compared with previous millimeter sensors. Preliminary millimeter dimension coplanar waveguide (CPW) sensors are tested for detection of saturated volatile organic chemical (VOC) vapor and the results show that polymer contribute to the output signal in comparison with sensors without polymer. Micrometer CPW sensors based on gold deposited silicon wafer are then tested. A limit of detection on the level of hundred ppmv and a response time of a minute are achieved.

5.2 Methods and Procedures

5.2.1 Polymer Coating

Based on the volumetric and swelling mechanism of polymers after absorbing VOC molecules, polymers are promising for high sensitivity and high selectivity detection of CWAs and TICs with the RF interferometer. Polymer coated on a sensor will experience a dielectric change caused by volumetric swelling, the molecules it absorbs, the molecular structure changes caused by the absorbents etc. in the presence of volatile molecules. Previous work has confirmed that polymers, such as polymer glycidyl methacrylate (PGMA), swell to different volume ratio to different VOC vapors and

polymers are successfully used to differentiate vapors in combination with optical devices [5.8].

PGMA is used as the absorbing layer for the experiments. The polymerization was carried out in methyl ethyl ketone (MEK) at 45 °C. Azobis was used as an initiator. The polymer so obtained was purified by multiple precipitations from MEK solution in diethyl ether. To obtain PGMA films, PGMA was dissolved in MEK at different concentrations and thin films were deposited on the substrate by dip coating after cleaning the sensor. After dip coating process, the sensors are annealed for hours to strengthen the polymer coated.

5.2.2 Gas Dilution System

Some common VOC including: acetone, ethanol, methanol and isopropyl alcohol, are tested to evaluate the capability of the proposed method for measuring CWAs and TICs. In order to achieve low concentration VOC vapor, a gas dilution system is designed with its schematic shown in Fig. 5.1 (a) and built as in Fig. 5.1 (b). VOC liquid sample is kept in a closed glass bottle at constant temperature provided by a thermal bath. The vapor pressure of the VOC can be found with regard to the temperature, which could be further used to calculate the exact concentration diluted with carrier nitrogen. The thermal bath is set to a temperature near room temperature in order to avoid concentration changes caused by heat transfer after the vapor enters the tube. After sufficient headspace time, a first flow of high purity nitrogen, used as carrier gas, was controlled by one mass flow controller (MFC) of full scale 0–10 ml/min and let into the vapor container by

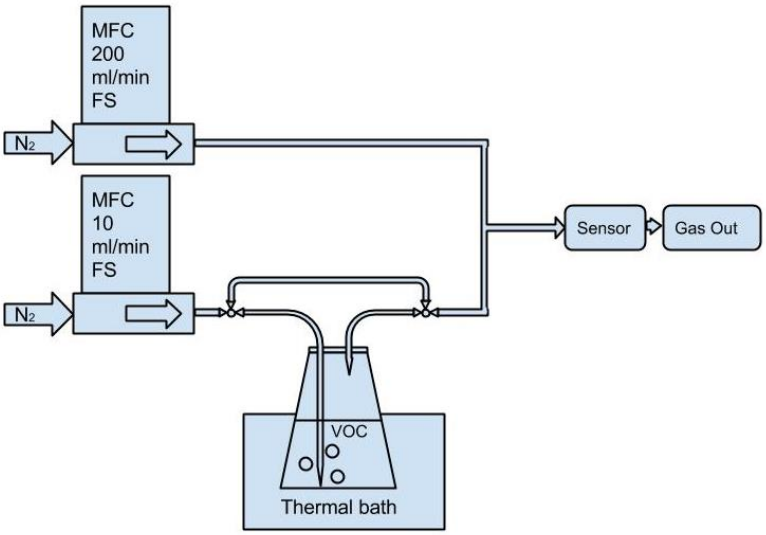

(a)

(b)

Fig. 5.1 The schematic of the gas dilution system.

opening the valves manually. The VOC was then diluted with a second flow of air controlled by the other MFC of full scale 0–200 ml/min and then transported to the chamber where the polymer coated sensor was placed. Another MFC with full scale of 0-10 L could be included into the system to give even lower concentration. The vapor flow

goes out in the other end to the ambient environment after rinsing the polymer coated surface.

The chamber was attached to the sensor by several wood pieces. The chamber is isolated to the ambient environment by an O-ring, which provides excellent air isolation and electrical isolation as well. The tubes are mainly made from copper and brass, which are compatible with VOCs to test including acetone, methanol, ethanol etc. The system could dilute common VOCs to a concentration level of hundred ppmv and CWA simulants to a level of ppbv with high accuracy since the accuracy of MFC is guaranteed with a flow rate higher than 10% of its full scale.

5.2.3 RF sensors design

For the purpose of increasing RF interferometer sensitivity, we design three sensors CPW based structure. The sensitivity of the RF sensor gets higher as the feature size of the sensor gets smaller. However, the current sensor fabrication techniques stop at micrometer level, which is popularly referred to as microelectromechanical systems (MEMS). Therefore, the sensors designed are based on 10 micrometer technique, which is the minimum size most micro-fabrication companies could handle. The substrate is fused silica with a thickness of 1mm, which is a high frequency dielectric material. The deposited gold is 2 um. The total size of the sensor is 2” * 0.5” and the schematics of the sensors are shown as figure 5.2.

The CPW in the first layout of Fig. 5.2 is a traditional CPW with 0.5” micrometer sensing length to accommodate the size of the gas chamber. The width and gap of the

micrometer part is 3.2 mil and 0.4 mil respectively. In order to increase the sensing area, the mitered structure CPW is designed as shown in the second layout of Fig. 5.2. Five zigzags are used to increase the sensing length by 6 times, which could increase the sensitivity by around 5 times. Corners are trimmed to guarantee transmission coefficient. The third layout in Fig. 5.2 is a CPW IDC which is the most popular structure for low frequency electrical sensors. A zoom-in view shows the interdigital fingers of the IDC, which has 32 pairs of fingers. And it would be interesting to test the IDC to compare to transmission structures such as the CPWs. The transmission coefficients are summarized in Fig. 5. 3 and we can see that the sensors have acceptable $|S_{21}|$ in a wide frequency range.

We use simulation software and analytical equations to obtain expected response. HFSS is used for simulation and importing meshes is used between the same models with different dielectric to remove the effect of mesh and the simulation results are only results of polymer dielectric. In analytical analysis, conformal mapping is used for calculation. The polymer on the metal is not considered since it is too thin compared to the metal width. Only the polymer in between the gaps of the CPW is used for analytical calculation. In evaluation, the dielectric constant of polymer is changed from 2.1 to 2.5, which is reasonable in terms of polymer. The exact geometrical parameters are used as in the designs. For micrometer CPW equations give 0.1082° phase change and simulation gives 0.0811° phase change at 10 GHz. The analysis helps explain the fundamental of the signal detected and it could be used to deduce polymer volumetric swelling in the future experiments.

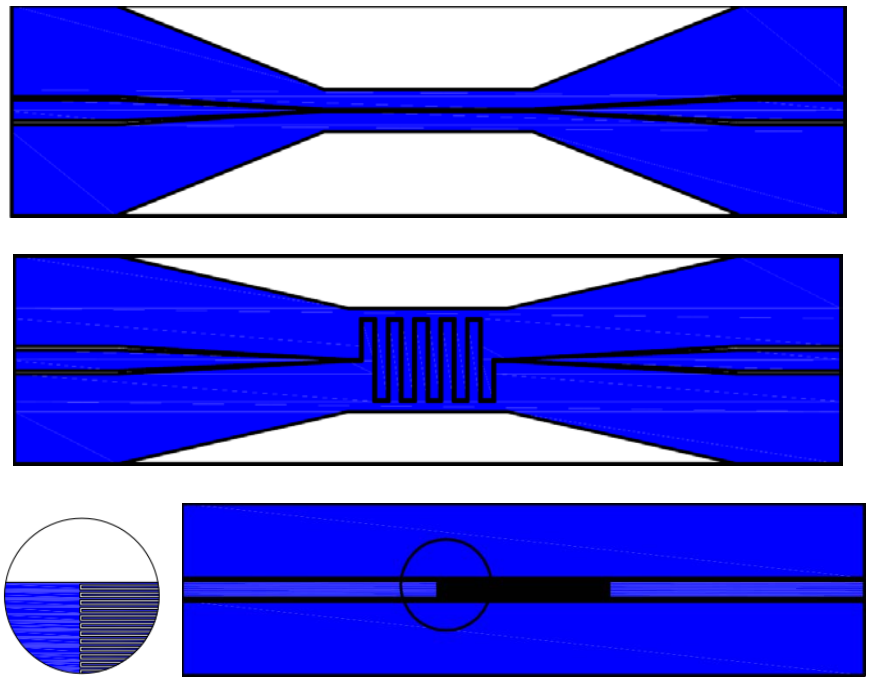

Figure 5.2. The layout of the sensors.

5.2.4 Vapor effect considerations

The goal of the project is to maximize the effect of polymer. However, VOC vapors might affect the measurement results as well as it fills the whole chamber expect the polymer, especially when the interferometer is highly sensitive. From published results in the past, we believe that the VOC vapor in the chamber will not affect the RF interferometer signal for two reasons. Firstly, the dielectric of VOC vapor is much lower than making a weighted sum of the liquid vapor sample and the carrier gas by their parts. For example, the permittivity of saturated water vapor from publication is only 1.000167 at room temperature. Besides, a value on the 4th digit is below the limit of detection the RF interferometer could distinguish from carrier gas. Thus, we can deduce that, for other

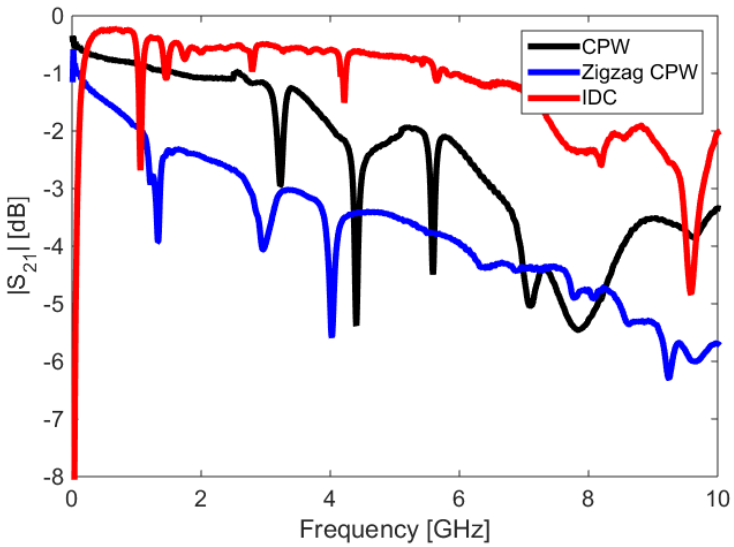

Figure 5.3. The measured transmission coefficients of the sensors.

common VOCs used in our experiments, they have little effect on the RF output signal as well. Another reason that vapor has little effect is that all reported electronics gas detectors that exploited similar feature size, such as, conducting metal width and vapor and polymer thickness, did not mention the vapor effect to their measurement results. For the above two reasons, we can say that vapor does not contribute to the measured results of interferometer, awaiting further experiments to validate.

5.3 Results and Discussions

5.3.1 Preliminary results with millimeter CPW sensors

The first group of experiments is carried out on millimeter feature size CPW sensors to preliminarily evaluate the RF interferometer method of detecting VOCs. The CPW is covered all over with PGMA, whose thickness is around 100 nm. The length,

width and gap of the CPW are 50.8mm, 1.4 mm and 0.152 mm, respectively, and the substrate is Duroid 5870. Saturated vapor is tested for the experiments by injecting VOC liquid into the chamber through the silicone tube. The chamber is simply made from a plastic petri dish, which has the problem of leakage.

The RF interferometer system is adjusted to a level of below -85 dB and the stability is assured before injecting the VOC liquid. As soon as the liquid is injected, we began to record data every half a minute. Figure 5.4 plots the figure shifting process with time at one minute interval after acetone is injected. As can be seen, the frequency of $|S_{21}|_{min}$ shifts right as the polymer absorbs the vapor. An almost real-time response is observed. Due to the effect of external noise, only frequency information is trustworthy for analysis purpose, since the amplitude changes caused by the vapor is smaller than the effects of noise. The lid of the chamber is opened at 10 minutes after injection and the time is sufficient for all VOCs used to reach to the state of saturation. All measurement results show that the frequency shifts to the starting point before vapor is formed in the chamber. This confirms that the signal observed is caused by the VOC vapor.

Five VOCs are measured: acetone, methanol, ethanol, hexane and isopropyl alcohol (IPA). In order to evaluate to what extent PGMA contributes to the frequency shift, measurements are also carried out with uncoated CPW in exactly the same setup.

Table 5.1 summarizes the maximum frequency shift of the two different setups and the time it takes to reach saturation. From the data, we could conclude that the RF interferometer has a larger frequency shift with polymer coated sensors that uncoated sensors and the sensing system has an almost real-time response. It indicates that the

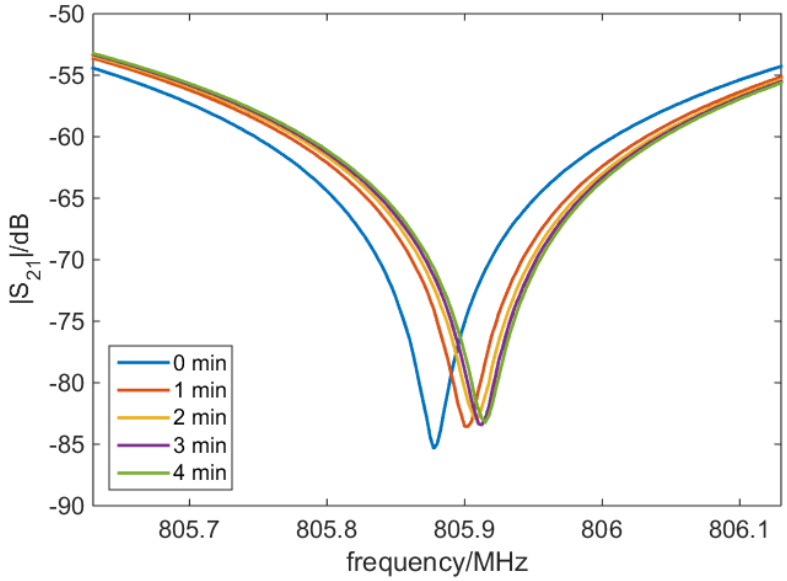

Figure 5.4. Measured RF signal at different times after VOC liquids are injected into the chamber.

polymer absorbing the VOC molecules could help us identify different VOCs. However, different from the published results from other groups that vapor alone does not affect the electric signal, we observed frequency shift with uncoated CPW sensor. We believe it is caused by the phenomenon that VOC molecules are attached to the Duroid substrate, which is a kind of polymer. In order to maximize the PGMA effect and remove the vapor effect on the RF signal, other sensors are designed and tested with the substrate of glass.

5.3.2. Results with micrometer CPW sensors

Theoretically, the sensitivity of RF sensor increases as the feature size of the sensor decreases. Therefore, we use micrometer CPW for the second group of measurements with the gas dilution system. Before starting doing measurements, we have

Table 5.1

Summary of preliminary measurement results

VOCs	Δf/KHz with polymer	Δf/KHz W/O polymer	Response time/min
Acetone	40	30	5
Methanol	12.5	7.5	4
Ethanol	-17.5	-10	6
Hexane	7.5	2.5	3.5
IPA	2.5	0	3

checked with soap water that all connecting parts of the gas dilution system are intact. We also double checked with another mass flow meter that the total flow at the output end equals the sum of the flow rates of the two MFCs. The thermal bath is set to a temperature of 22°C closer to room temperature to avoid thermal exchange in the tubing part. The RF interferometer was tuned to below -85 dB before the valves are open. The measurement system is assured to be stable before experiment. A MATLAB program is run to record $|S_{21}|$ trace automatically every 6 seconds. Each measurement lasts 6 minutes and the valves are open at the beginning and shut off at 3 minutes. 2000 and 5000 ppmv concentrations are tested for acetone and ethanol for all three sensors at 3 different

frequencies ranging from 1 GHz to 8 GHz. Each measurement is repeated twice. Totally 72 measurements are conducted. An IFBW of 100 Hz and span of 500 KHz are used.

Fig. 5.5 is one measured result with 500 ppmv acetone at 7.469 GHz. From measurement results, we can see that the RF interferometer could detect acetone at a level of hundreds ppmv and have a response time less than a minute. After 200 seconds, gas with acetone travels to the chamber and the frequency of $|\boldsymbol{S}_{21}|_{\min}$ shifts left. After the same amount of time after closing the valves, the curve returns to the starting position and this proves that the changes measured are caused by the gas with acetone.

The obtained results of frequency shifts are summarized in Fig. 5.6 for 2000 and 5000 ppmv acetone and ethanol. From the results, we can see that the IDC has similar sensitivity to that of CPW and the meandered CPW has the strongest sensitivity since it has the largest interaction area for the same chamber. We can also see that as frequency increases, the sensitivity increases due to a longer electrical length. 5000 ppmv causes larger response than 2000 ppmv and we can use this information to obtain the concentration from measurement results. Also, the two tested chemicals showed different patterns for different devices and this information is potential to distinguish chemicals As for the limit of detection, hundreds of ppmv has been shown achieved as in Fig. 5.5. This limit of detection is comparable to other electrical methods detecting VOCs and it is possible that we can have better results by using the high sensitive polymer.

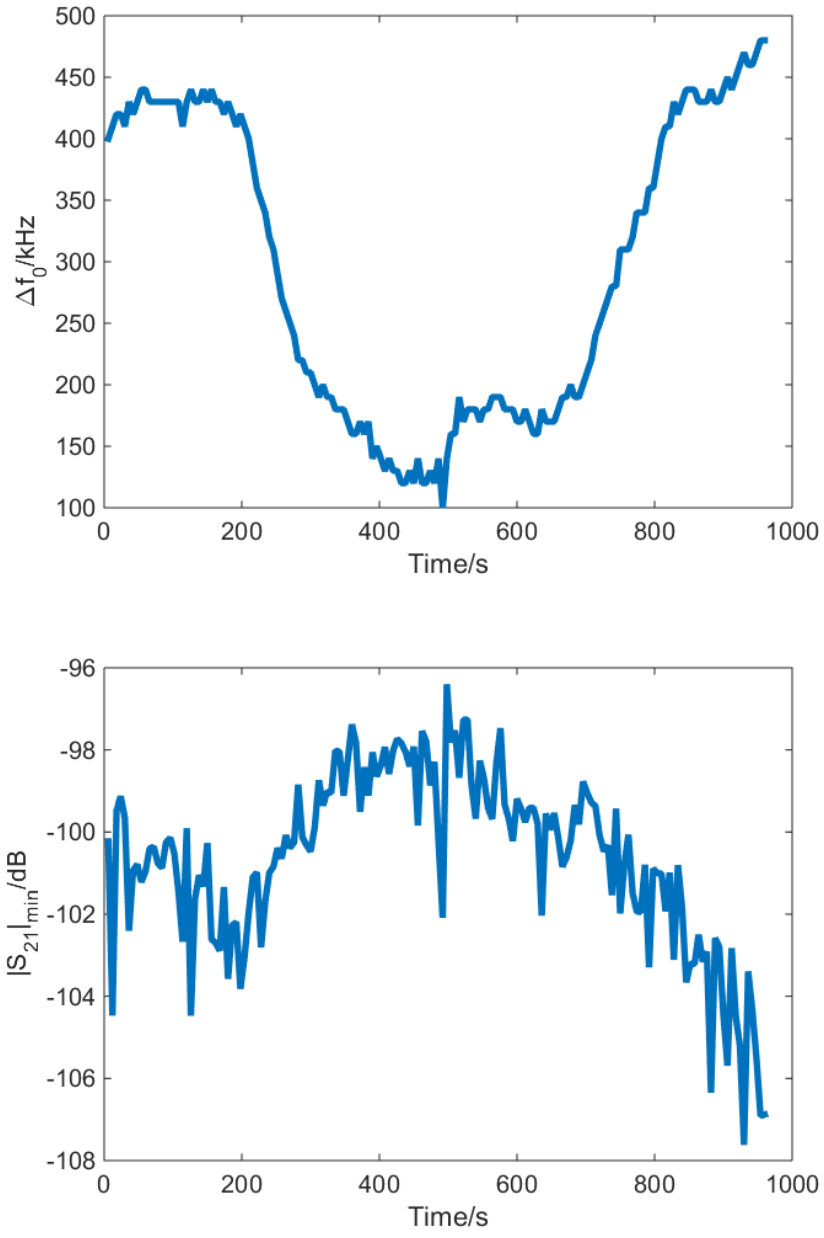

Figure 5.5. $|\boldsymbol{S}_{21}|$min changing with time for 500 ppmv acetone at 7.469 GHz.

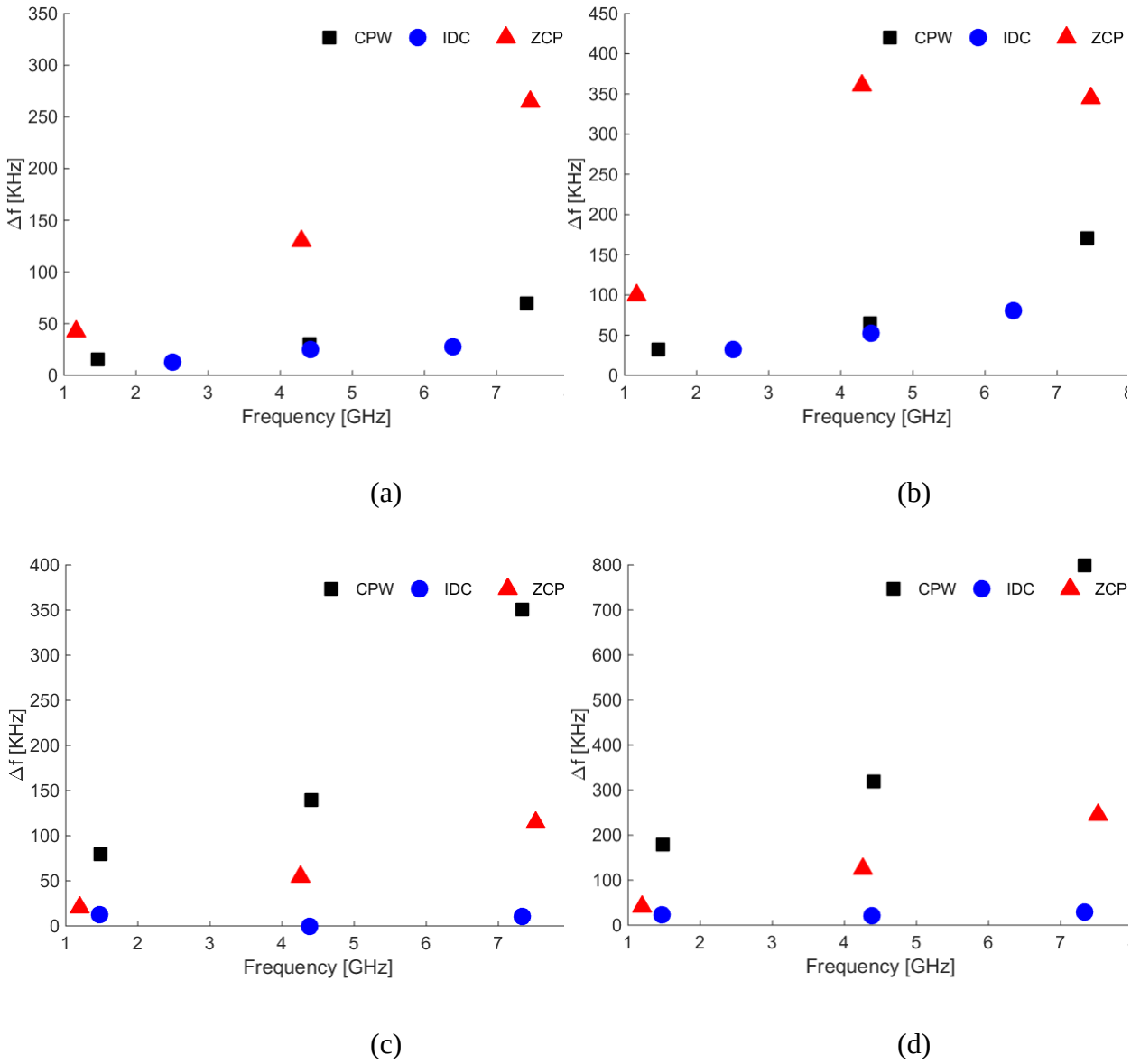

Figure 5.6. Summarized frequency shift (a) 2000 ppmv acetone; (b) 5000 ppmv acetone; (c) 2000 ppmv ethanol; (d) 5000 ppmv ethanol.

REFERENCES

[5.1] Zimmermann, Céline, et al. "A love-wave gas sensor coated with functionalized polysiloxane for sensing organophosphorus compounds." *Sensors and Actuators B: Chemical* 76.1 (2001): 86-94.

[5.2] Matatagui, D., et al. "Array of Love-wave sensors based on quartz/Novolac to detect CWA simulants." *Talanta* 85.3 (2011): 1442-1447.

[5.3] Mlsna, Todd E., et al. "Chemicapacitive microsensors for chemical warfare agent and toxic industrial chemical detection." *Sensors and Actuators B: Chemical* 116.1 (2006): 192-201.

[5.4] Kitsara, M., et al. "Single chip interdigitated electrode capacitive chemical sensor arrays." *Sensors and Actuators B: Chemical* 127.1 (2007): 186-192.

[5.5] Potyrailo, Radislav A., and William G. Morris. "Multianalyte chemical identification and quantitation using a single radio frequency identification sensor." *Analytical chemistry* 79.1 (2007): 45-51.

[5.6] Rossignol, J., et al. "Microwave-based gas sensor with phthalocyanine film at room temperature." *Sensors and Actuators B: Chemical* 189 (2013): 213-216.

[5.7] Zarifi, Mohammad H., et al. "Microbead-assisted high resolution microwave planar ring resonator for organic-vapor sensing." *Applied Physics Letters* 106.6 (2015): 062903.

[5.8] Giammarco, James, et al. "Towards universal enrichment nanocoating for IR-ATR waveguides." *Chemical Communications* 47.32 (2011): 9104-9106.

CHAPTER SIX

SUMMARY

In this work, the additive RF interferometer is investigated. Different aspects on how the RF interferometer works are described: an analytical model is given to relate the broadband response to the phase difference; the model relates measurement results including frequency and magnitude shift to MUT properties; more general situations of the interferometer are discussed. The analysis of single particle passing over a coplanar waveguide in microfluidic channel is presented and combined with the RF interferometer model to validate a group of measurement results. The solution given might be applied to single cell measurement. Then the RF interferometer sensitivity is enhanced by incorporating filters and functionally expanded by using the reflection coefficients at the same time with transmission coefficients. In the end, an application of measuring gas with the RF interferometer is presented. The gas dilution system is built and connected to the interferometer and preliminary results are presented.

The interferometer has demonstrated great sensitivity performance in multiple measurement applications. Future effort will be focused on quantifying the detection results with the designed filters. As for the gas measurements, new highly sensitive polymer will be tested to find the limit of detection of the built sensors. Multi branches interferometers are found be very sensitive and this technique might help in improving the sensitivity as well.